2016

Experimental Investigation of Turbulent Flow Induced by New-Generation Wind Fences with Multi-scale Fractal Structure

Sarah M. Mcclure

Recommended Citation

Mcclure, Sarah M., "Experimental Investigation of Turbulent Flow Induced by New-Generation Wind Fences with Multi-scale Fractal Structure" (2016). *ETD Archive*. 911.
https://engagedscholarship.csuohio.edu/etdarchive/911

SARAH M. MCCLURE

Bachelor of Science in Mechanical Engineering

Cleveland State University

May 2014

submitted in partial fulfillment of requirements for the degree

MASTER OF SCIENCE IN MECHANICAL ENGINEERING

at the

CLEVELAND STATE UNIVERSITY

May 2016

We hereby approve this Master's thesis

For

Sarah M. McClure

Candidate for the Master of Science in Mechanical Engineering degree

for the Department of Mechanical Engineering

And

CLEVELAND STATE UNIVERSITY'S

College of Graduate Studies by

____

Dr. Wei Zhang, Ph.D.

____

Department & Date

____

Dr. Mounir Ibrahim, Ph.D.

____

Department & Date

____

Dr. Petru Fodor, Ph.D.

____

Department & Date

05-09-2016

Student's Date of Defense

ACKNOWLEDGEMENTS

The author wishes to acknowledge the following:

My mother Constance McClure, for supporting me throughout my education. Without your support I would not have been able to accomplish what I have done in the past two years for my master’s study. Also, thank you for your visit to South Korea as a familiar face was much needed after being far away from home for a long time, for the first time in my life.

My advisor, Dr. Wei Zhang for her help throughout my master’s study. All her advice, guidance and support has pushed me to finish my degree, pursue my interests and strive to be the best in doing so.

Dr. Mounir Ibrahim for his support for the two years, his words of encouragement and laughter at difficult times.

I greatly acknowledge the support funded by the East Asia and Pacific Summer Institute Program Awarded by the National Science Foundation. With this support I gained a wealth of knowledge outside the US which strengthened my goals academically. Also, it gave me a chance to face different challenges, explore a part of the other side of the world, interact with people from another culture and a renewed appreciation of the opportunities available in America.

Professor Sang-Joon Lee and POSTECH BBRC lab students, thank you for sharing your knowledge with me and helping me to conduct my experiments successfully. Also, thank you all for inviting me to participate in your research group meetings, lunches/dinner and hiking activities.

EXPERIMENTAL INVESTIGATION OF TURBULENT FLOW INDUCED BY NEW-GENERATION WIND FENCES WITH MULTI-SCALE FRACTAL STRUCTURE

SARAH MCCLURE

ABSTRACT

Understanding and controlling atmospheric boundary-layer flows with engineered structures, such as porous wind fences or windbreaks, has been of great interest to the fluid mechanics and wind engineering community. Previous studies found that the regular mono-scale grid fence of 50% porosity and a bottom gap of 10% of the fence height are considered to be optimal over a flat surface. Significant differences in turbulent flow structure have recently been noted behind multi-scale fractal wind fences, even with the same porosity. In this study, wind-tunnel tests on the turbulent flow and the turbulence kinetic energy transport of 1D and 2D multi-scale fractal fences under an atmospheric boundary-layer flow condition were conducted. Velocity fields around the fractal fences were systematically measured using PIV to explore the turbulent flow around the fences at the Reynolds number of approximately $3.6\text{x}10^4$ based on the free-stream speed and the fence height. The turbulent flow structures induced by specific 1D/2D multi-scale fractal wind fences were compared to those of a 2D conventional mono-scale grid fence. In addition, each wind fences performance on wind speed reduction and sheltering effect were evaluated to determine the effectiveness of the fractal versus mono-scale grid geometries. Among the three wind fences, leeward of the fence, the 2D fractal fence is the most effective in reducing the incoming wind speed showing a maximum wind speed reduction coefficient of 0.90. Also, the 2D fractal reveals the most impressive shelter zone consisting of a magnitude of 0.40 ranging from x = 1.5H to 4.5H. Near the surface, the Reynolds shear stresses are very high for the conventional and 2D fractal fence, which is an indicator of potential particle remobilization. In contrast, the 1D fractal fence has the lowest Reynolds shear stress near the surface, which suggests the 1D fractal fence may be better in preventing particle remobilization from excessive turbulent stresses. The present results can contribute to optimizing the design for new-generation wind fences to reduce oncoming wind velocities and help snow/sand particle deposition on critical infrastructure such as roads and bridges.

TABLE OF CONTENTS

CHAPTER

APPENDIX A

APPENDIX B

LIST OF TABLES

LIST OF FIGURES

NOMENCLATURE

1D/2D	one dimensional/two dimensional
α	Power-law exponent or attack angle
ABL	Atmospheric boundary layer
B	Number of fractal pattern iterations
D_f	Fractal dimension
dt	Time interval between two frames
η	Porosity
fps	Frames per second
H	Height of fence or height of wind tunnel test section
K	Turbulence kinetic energy, $\frac{1}{2}\left(\overline{u'^2(x, y)}+\overline{v'^2(x, y)}\right)$
l	Characteristic length scale
L	Length of wind tunnel test section
m/s	Meters per second
N	Number of fractal pattern iterations or sample size
PIV	Particle Image Velocimetry
Re	Reynolds number, $\frac{U_0 * l}{\upsilon}$
RSS	Reynolds shear stress, $\frac{-\overline{u'(x,y)v'(x,y)}}{{U_0}^2}$
R_t	Ratio of the bar’s successive iteration thickness
$Rc_{\Delta x,y}$	Wind-speed reduction parameter
$\sigma(u_0)$	Standard deviation of undisturbed flow
t	Time

Tu	Streamwise turbulence intensity, $\frac{u_{rms}}{U_0}$
Tv	Vertical turbulence intensity, $\frac{v_{rms}}{U_0}$
t_{max}	Maximum bar thickness
U_0	Reference velocity or oncoming flow speed
U	Ensemble averaged streamwise velocity
μs	Micro-seconds
u_i'	Streamwise velocity fluctuations
u_j'	Vertical velocity fluctuations
$u(x)$ or $u_i(x)$	Local streamwise velocity
u_{rms} or $\sigma(u)$	Root-mean-square of local streamwise velocities
V	Ensemble average vertical velocity
$v(x)$ or $u_j(x)$	Local vertical velocity
v_{rms} or $\sigma(v)$	Root-mean-square of local vertical velocities
υ	Kinematic viscosity
W	Width of fence or width of wind tunnel test section
Δx	Streamwise distance windward or leeward of the fence
x	Horizontal Cartesian coordinate
y_0	Reference height
y	Vertical Cartesian coordinate
Δy	Height above the ground surface along the fence height

CHAPTER I

INTRODUCTION

1.1. Background and significance of wind fence

In past centuries and in the present day, natural or artificial objects are strategically placed to reduce high oncoming wind speeds for the protection of crops, homes, soil erosions and to also control snow or sand drifts near roadways, and are sometimes referred to as windbreaks or shelterbelts. Natural windbreaks such as trees, shrubs, and grasses originated in the mid-1400's, protecting agricultural production to being widely used throughout the world to provide crops, livestock, and wildlife habitats protection from vigorous winds and to control wind erosion and blowing snow (Brandle et al., 2004). Artificial windbreaks such as porous fences shown in Figure 1, provide people similar protection reducing hazardous winds to control snow or sand drifts and have been systemically studied for optimal design and cost-effectiveness since the 1940's (Dong et al., 2011). Typically, if a fence is used for the purpose of reducing wind speed and to protect objects in a downwind shelter zone, then the structure is referred to as a wind fence (Bailiang and Sherman, 2015).

Significant research on wind fences demonstrated their importance and emphasized their benefits. In the 1960's, research conducted on fences used for snow drift control by the US Forest Service began, and was used to report effective guidelines for wind or snow fences to control snow drifts off roadways in the 1970's (Tabler, 1994). A 10-year Wyoming case study implementing such guidelines of the research to diminish a huge drifting problem affecting drivers on Interstate Highway I-80, highlighted the importance and increasing benefits found over time. The outcome of the reduced snowdrifts near I-80 significantly lowered winter maintenance costs from 33% to 50%, reduced road surface pavement conditions, increased driver visibility and decreased accidents (Tabler, 1994).

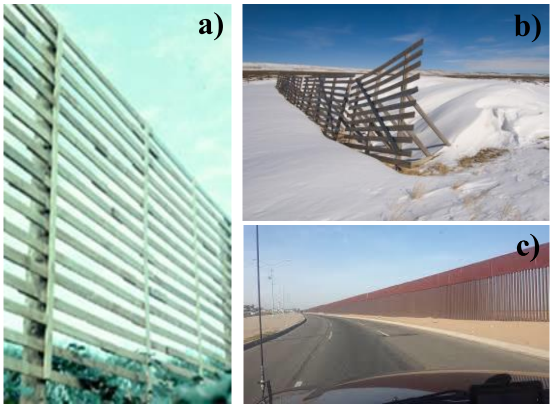

Figure 1: Conventional (typical) porous fences a) wind fence, b) snow fence and c) sand fence

Since trapping snow with fences was proven to reduce mechanical snow removal costs by 100 times, it grew increasingly popular among researchers to conduct further studies on properly engineering and placing snow or wind fences, to maximize their effectiveness (Tabler, 1991).

1.2. Parameters of wind fence

Research work has highlighted the functional effects of windbreak structure on incoming wind velocities and how their structural characteristics impact the flow. For windbreaks that are long with respect to their height, such as wind fences, the most important structural parameter on the wind flow is porosity (Heisler, 1988). Porosity is the ratio of the open area to the total area of the fence, including the bottom gap between the fence and ground. Porous fences are the most common type of wind fence as their primary purpose is to extract adequate energy from the oncoming flow to improve control of particle deposition while preventing excessive turbulent stresses from causing particle remobilization leeward of the fence (Keylock et al., 2012). In general, porosity, height, and orientation or location of wind fences are the main parameters that control their effectiveness (Norman, 1985). In addition, a wind fence effectiveness is determined from the magnitude of wind speed reductions and turbulence intensities (Dierickx, 2003).

Maximum wind velocity deficits leeward of the fence is closely related to its porosity (Heisler, 1988). Previous studies stated that relatively low porosity windbreaks between 20%-35% produced the maximum reductions of the incoming wind speeds that also created more turbulent fluctuations downstream, which resulted in faster recovery of the mean flow (Raine and Stevenson, 1977). More recent studies confirmed that decreasing fence porosity, decreases the mean streamwise velocity behind the fence and greatly increases the velocity fluctuations in the vertical direction along the fence height (Dong et al., 2011).

Aside from porosity, the other main important structural design parameter is the wind fence height and height of the bottom gap. The height of the fence influences the cost,

Figure 2: Structural design parameters for wind fence

controls the distance of the wind flow effects leeward of the fence and trapping efficiency in the case of a snow fence (Tabler, 1991). The bottom gap of such fences prevent buildup of particles, snow or sand, in front of the fence reducing damages to the fence caused over accumulation (Tabler, 1994). Figure 2 illustrates the structural parameters of the height, bottom gap and porous regions of a wind fence.

Lastly, the orientation or location of a wind or snow fence affect its functionality and overall effectiveness. A fences orientation is defined by its perpendicular alignment with respect to the dominant direction of snow transport (Tabler, 1994). The angle between the winds transport direction and its perpendicular alignment to the fence is called the attack angle, α (Tabler, 1994), illustrated in Figure 3. The effectiveness of wind fences to prevent particle transport decrease as the distance between the road and the fence increases when the prevailing direction of the wind is not perpendicular to the fence (Tabler, 1994). Therefore, strategic placement of wind fences is imperative in maximizing its effectiveness.

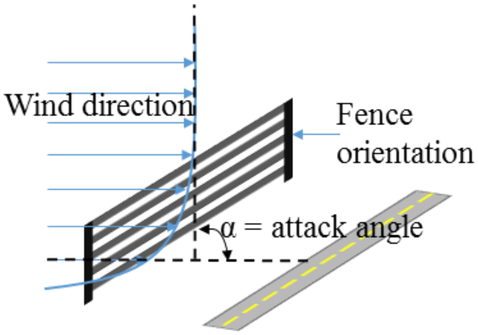

Figure 3: Illustration of fence orientation and attack angle.

1.3. Optimal design parameters of wind fence on level terrain

The validity of accurately defining optimal design parameters for full-scale windbreak performances was confirmed through wind tunnel experiments using model wind fences within various simulated atmospheric boundary layer conditions (Raine and Stevenson, 1977). Since then, several experimental investigations in atmospheric boundary layer wind-tunnels simulating turbulent flows over smooth and rough surfaces have determined optimal parameters for two-dimensional porous wind fences (Perera, 1981; Dierickx et al., 2003; Lee and Kim, 1999; Kim and Lee, 2002).

The specifications of the design of wind fences depend mainly on the height and optimal porosity parameters. The height of wind fences is proportional to the horizontal extent of the wind speed reductions and the porosity controls the magnitude of the wind speed reductions (Heisler, 1988). Previous studies found that a mono-scale grid fence of 50% porosity and a bottom gap of 10% of the fence height are considered to be optimal parameters over a flat surface (Tabler, 1980; Tabler, 1991). Therefore, to expand our knowledge even further on increasing wind fence effectiveness, this experimental study has adopted those optimal parameters of a wind fence over a level terrain and applied them to multi-scale fractal wind fence design models for comparison against a two-dimensional (2D) conventional mono-scale wind fence design model.

1.4. Fractal wind fences

In short, fractals are a body made of parts similar to the whole at reduced length scales or objects containing infinitely decreasing repeated identical shapes of itself. Observations of fractal geometry appear in a wide variety of irregular phenomena readily found in nature

Figure 4: Fractals in nature a) clouds, b) snowflakes, c) river networks and d) trees.

(Debnath, 2006). For instance, complex fractal geometries in nature appear within clouds, river networks, trees and snowflakes shown in Figure 4. In the case of a tree, its primary structure is comprised of a tree trunk with the largest branches. Stemming from the branches are smaller branches to even smaller branches then to the smallest scale which are the stems budding leaves. The reduction of the largest branches to the stems budding leaves is an example of the reduction of parts similar to whole tree itself. However, some fractals contain self-similarity with subsequent generations reduced by a fixed length scale ratio to the parent generation which can be expressed by simple mathematical expressions (Kang, 2011).

Fractal objects have been experimentally and theoretically reported to produce high turbulence intensities which then rapidly decay within the near wake region (Seoud and Vassilicos, 2007; Hurst and Vassilicos, 2007; Kang, et.al, 2011). Turbulent flows generated by multi-scale fractal structures to alter the nature of atmospheric boundary layer turbulence are of a recent topic to the fluid mechanics community.

A recent publication was the first to highlight the detail of the wake structure behind one-dimensional (1D) multi-scale fractal porous wind fences with constant porosity in a boundary layer, which showed significant changes to the turbulent structure opposed to mono-scale or conventional 1D porous fences of the same porosity (Keylock, et al., 2012). The study highlighted the increased streamwise turbulence intensity in the near wake region compared to the 1D conventional fences of the same porosity. This discovery demonstrated the promising potential of fractal fences to achieve improved control of boundary-layer turbulence and possibilities in increasing wind fence effectiveness.

Therefore, it is important to study how porous wind fences implementing different fractal geometries affect various oncoming flows.

1.5. Purpose of research

Previous studies found that the conventional mono-scale grid fence of 50% porosity and a bottom gap of 10% of the fence height are considered to be optimal parameters for a wind fence on a flat surface. In addition, significant differences in turbulent flow structure have recently been noted behind multi-scale fractal wind fences, even with the same porosity. This is of great interest for wind control studies as alterations to atmospheric turbulence can be used to reduce strong winds, enhance deposition of snow or sand particle suspension or saltation, and influence pollutant dispersal (Keylock, et al., 2012).

Keylock et al., (2012) investigated the induced flow structure past 1D multi-scale fractal porous wind fences compared to conventional mono-scale porous grid fences of the same porosity. Immediate conclusions from the study state that specifying only the height, bottom gap size and porosity parameters are not enough in determining the wake structure of turbulence, such that the arrangement of the struts also have an effect. Higher turbulence production and dissipations rates were seen for the multi-scale forced flow rather than fences that forced the flow in a more traditional manner. Thus, their findings highlighted the potential of using multi-scale fractal geometries for optimization of wind fence designs to control for production or dissipation of turbulence intensity depending on the application. Therefore, the purpose of this research was to expand upon the previous study, constructing a replica of the 1D multi-scale fractal wind fence to compare the behavior of the multi-scale flow past a 2D multi-scale fractal fence wind fence, consisting of the optimal parameters over a flat surface, to advance our knowledge even further on optimizing such wind altering structures.

In this study, wind tunnel tests on the turbulent flow and the turbulence kinetic energy transport of 1D and 2D multi-scale fractal fences within an atmospheric boundary-layer over an open flat terrain were conducted. The experimental tests were conducted in an atmospheric boundary layer wind tunnel at Pohang University of Science and Technology in South Korea. The turbulent flow structures induced by specific 1D/2D multi-scale fractal wind fences were compared to those of a conventional grid fence. Velocity fields around the fractal fences were systematically measured using 2D2C PIV to uncover effects of key parameters on turbulent flows around the fences at the Reynolds number of approximately 3.6×10^4 based on the free-stream speed and the fence height. The mean flow fields captured experimentally were analyzed to investigate the differences in the turbulence generated, and to determine the effectiveness of each wind fence model. Furthermore, the present results would contribute to the design of new-generation wind fences around the world to reduce snow/sand deposition near critical infrastructure such as roads and bridges.

CHAPTER II

EXPERIMENTAL SETUP AND METHODS

2.1. Wind fence models

Three wind fence models, one conventional mono-scale grid fence and two consisting of multi-scale fractal geometries (1D and 2D) were designed and constructed for this study, shown in Figure 5. A detailed description of each of the wind fence design parameters are

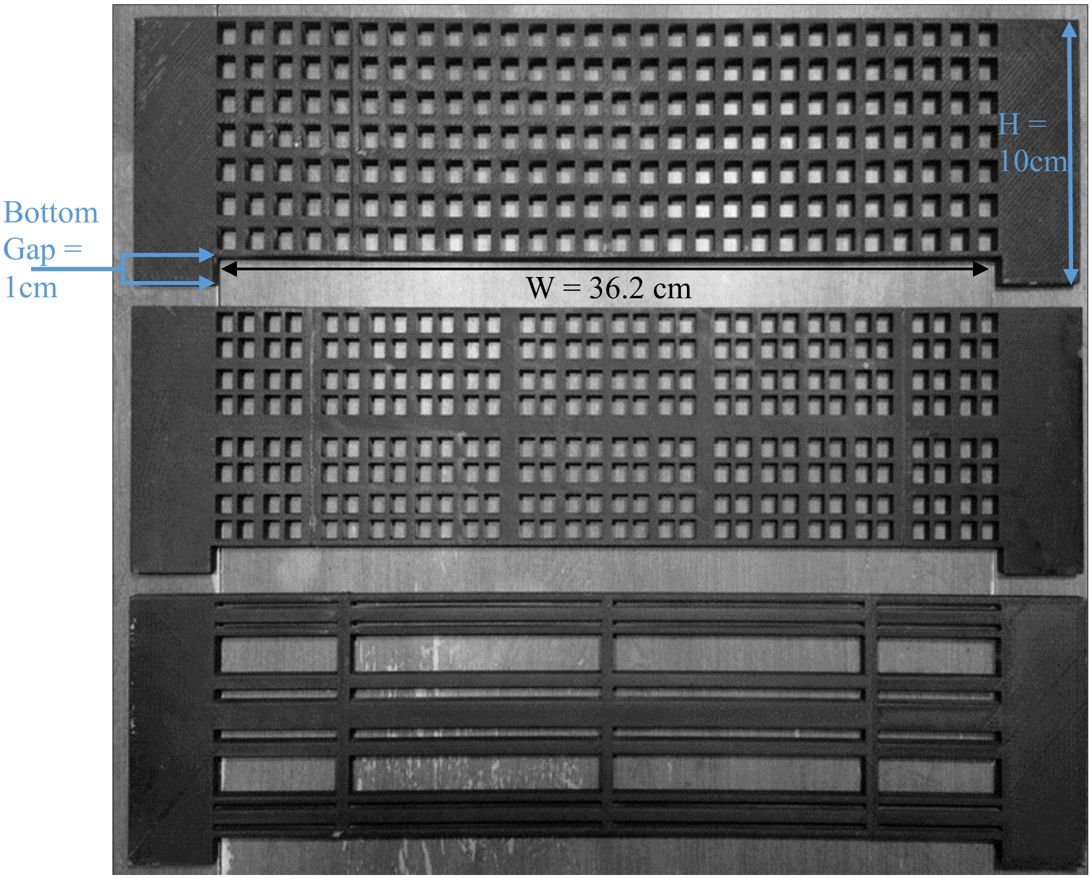

Figure 5: Wind fence models from top to bottom: Conventional fence, 2D fractal fence, and 1D fractal fence

outlined in Table I. The optimal design parameters for wind or snow fences over a flat terrain consisting of a porosity 50%, denoted as η in Table I, with a bottom gap of 0.1H (included in the porosity calculation), where H is the fence height, were chosen for each of the fence models (Keylock, et al., 2012; Tabler, 1991). In addition, since Keylock et al., (2012) based his fences off this criteria and it was imperative to match those dimensions of the 1D multi-scale fractal fence model of 50% porosity because it was replicated for this study, all of the three fence models in Figure 5 were designed for the same height, bottom gap height and thickness dimensions of 10cm, 1cm, and 7mm, respectively, to be consistent. Furthermore, all three fence models in Figure 5 were designed to have a width dimension of 36.2cm, for intended use of the wind tunnel at Cleveland State University; however, the experiments were not conducted there. The fence models were built using ABS plastic material in a Fortus250mc 3D printer with a slice height of 0.010 inch at Cleveland State University in room FH424. Additionally, mounts to stabilize and secure the models to the bed of the wind tunnel test section were created and 3D printed at the Biofluid and Biomimic Research Center at Pohang University of Science and Technology in South Korea. Moreover, the wind fence models were mounted perpendicular to the oncoming flow direction.

Table I: Wind fence design parameters

Wind fence design parameters:	**η (%)**	**N**	**R_t**	**R_L**	**B**	**D_f**	**t_r**	**t_0 (mm)**	**t_1 (mm)**	**t_2 (mm)**	**L_0 (mm)**	**L_1 (mm)**	**L_2 (mm)**
Conventional Fence:	50	1	1	0.5	4	2	1	4.23	--	--	--	--	--
2D Fractal Fence:	50	3	0.5	0.5	4	2	4	8.46	4.23	2.12	90	45	22.5
1D Fractal Fence:	50	3	0.5	--	4	2	--	10	5	2.5	--	--	--

2.1.1. Conventional fence

The conventional fence model is at the top of the three fences shown in Figure 5. In literature (Hurst and Vassilicos, 2007), the basic pattern of the conventional grid fence is geometrically known as a classical grid, where S = 2; $R_t = 1$; $R_L = 1/2$; $D_f = 2$ and $t_r = 1$, and is a special case of the cross grid fractal family which is defined by the number S of rectangular bars required, illustrated in Figure 6. The construction of the conventional grid geometry from the cross grid fractal generating pattern is demonstrated in the left schematic shown in Figure 7. The horizontal and vertical bar thicknesses t_0, are both equal where a=b for each iteration of the cross grid generating pattern, denoting that the bars successive iteration thickness is equal to one $R_t = 1$, as well as, the thickness ratio, $t_r = t_{max} / t_{min} = 1$; signifying the meaning of a mono-scale grid, previously stated. In addition, with L equal to the length of either vertical or horizontal rectangular bars, its successive iteration length is equal to ½ L (patterned four times, centered at each end of the cross; hence, $B = 4$ and $R_L = ½$, because the fractal dimension $D_f = \log(B)/\log(1/R_L) = 2$), (Hurst and Vassilicos, 2007).

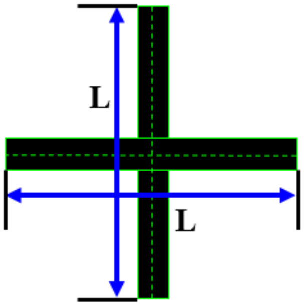

Figure 6: Cross grid fractal generating pattern, S = 2.

The distances between the two parallel struts where w=h in Figure 7, make the open areas of the conventional grid fence square spaces. The thickness of the struts are b = 4.23mm and the distance in between them taken from the centerline of the struts are w =

12.86mm, leaving the square space equal to w-b = 8.63mm. The conventional grid fence geometry is repeated for the entire length of the model fence and bounded within a frame consisting of a thickness equal to ½ b.

2.1.2. One-dimensional fractal fence

The one-dimensional (1D) multi-scale fractal fence model is at the bottom of the fences shown in Figure 5. The 1D fractal parameters were taken from the work done by Keylock et al., (2012). The 1D fractal is created by dividing the height of the fence, excluding the bottom gap, into six parts and removing the second and fifth part. This is repeated again for each of the three remaining solid parts, overall iterating the pattern a total of four times; hence, the number four is assigned for the parameter *B* in Table I, denoting how many times the fractal geometry is patterned. Creating the fractal in this manner makes the spacing of the gaps and the solid structure both multi-scaled; therefore, forcing the flow in a multi-scaled manner through the fence.

2.1.3. Two-dimensional fractal fence

The design of the two-dimensional (2D) fractal fence is among the cross grid fractal family S=2 shown in Figure 6. Iterations of subsequent generations of the cross grid fractal generating pattern about the vertical and horizontal planes, are reduced by a fixed length

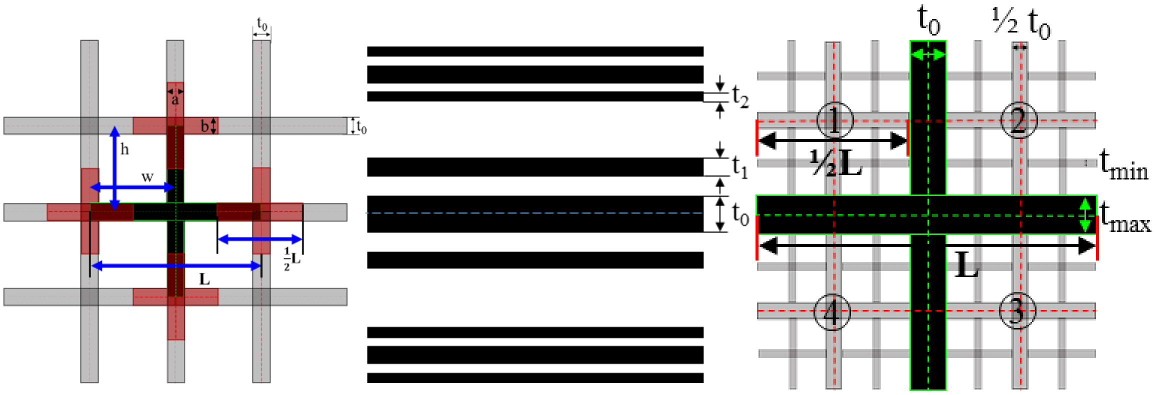

Figure 7: Side by side comparison of wind fence models from left to right: conventional, 1D fractal, and 2D fractal

scale ratio of ½, shown in the right schematic of Figure 7. A complete description for the cross grid fractal family requires at least four parameters, the fractal dimension D_f, number of iterations N, the thickness ratio of the maximum to minimum bar thicknesses $t_r = t_{max} / t_{min}$, and the ratio of the bar's successive iteration thickness R_t. Alike to the conventional fence, the voids in between the fractal grid structure of the fence are squares. Although, the open area of the square spaces are slightly smaller within the 2D fractal geometry than within the conventional grid fence geometry.

2.2. Atmospheric boundary layer flow simulation

Since atmospheric flows are turbulent in nature and it was desired to study the flow around wind fences in outdoor areas consisting of an open flat topography, an atmospheric boundary layer wind tunnel was needed. Therefore, experiments were performed in an atmospheric boundary layer wind tunnel with dimensions of 6.75m x 0.72m x 0.48m (L x W x H) consisting of laminar, transitional and fully developed turbulent regions at the Biofluid and Biomimic Research Center at Pohang University of Science and Technology

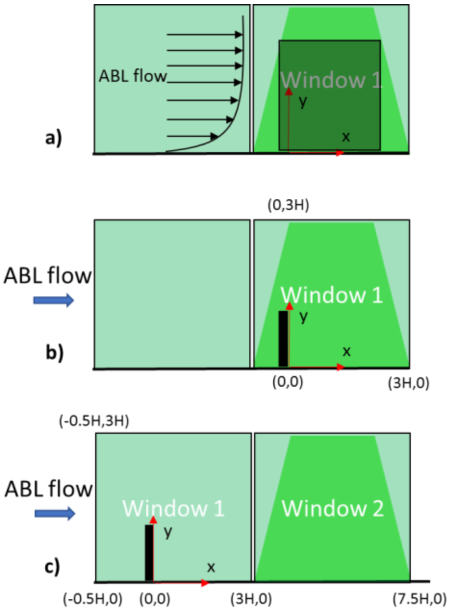

Figure 8: Schematic of PIV tests containing Cartesian coordinate system

in South Korea. As an atmospheric flow was needed to simulate flow over an open terrain, it was necessary to place roughness elements at the beginning of the test section and to conduct the experiments in the fully-developed turbulent region of the wind tunnel test section. Roughness elements such as spires of 0.28m in height and artificial grass with a fetch length of 0.5m were installed at the entrance of the test section to simulate an atmospheric boundary layer flow over a surface of uniform flat terrain. In addition, Particle Image Velocimetry (PIV) measurements were conducted along the centerline of the wind tunnel test section without any fence model, where only images of the undisturbed flow were acquired for two different oncoming wind speeds of 3.32 m/s and 5.53 m/s.

A schematic of the PIV experimental test plan for measuring the atmospheric simulated flow, along with the Cartesian coordinate system, is shown in Figure 8a. A total of 500 pairs of particle images were captured in three runs for each speed. Four hundred pairs of images were taken in two runs at a frame rate of 2.5 fps with the third run acquiring the last one hundred pairs of images at a frame rate of 2 fps. The resultant 500 instantaneous velocity fields were ensemble-averaged to obtain the undisturbed mean flow and turbulence field information for the two oncoming wind speed settings.

Since the experiment was performed in the fully developed turbulent region of the wind tunnel test section, the velocity profile entering and exiting the light sheet for the atmospheric boundary layer simulation was the same. Therefore, the center section of the ensemble-averaged flow field, starting from the surface to about one and a half times the boundary layer thickness, was averaged horizontally at each indexing height, for better results in uncovering the undisturbed mean flow and turbulence field information for the two oncoming wind speed settings. Vertical profiles of the atmospheric boundary layer mean flow properties such as, the streamwise and vertical velocities as well as, the mean turbulent statistics such as, the streamwise and vertical turbulent intensities, Reynolds shear stress and turbulence kinetic energy were analyzed and are shown in Figure 9a-f) respectively, for both oncoming wind speed settings.

Two speeds were tested because no matter the oncoming flow speed setting, the normalized velocity profiles of the simulated flow should match. The top plot of Figure 9 corresponds to the ensemble averaging of the total 500 instantaneous velocity fields taken for both oncoming wind speed settings. The bottom plot of Figure 9 corresponds to the ensemble averaging of 387 instantaneous velocity fields only for the oncoming flow speed setting of 5.53m/s, as there were 113 bad instantaneous flow fields for this experimental test run. After the removal of the bad instantaneous velocity fields, the vertical profiles of the two wind speed settings show better matching.

The uncovered mean streamwise and vertical velocity profiles of the simulated oncoming flows are shown in Figure 9a) and b), respectively. The mean streamwise velocity U and mean vertical velocity V, were normalized by the oncoming flow speed U_0, versus its corresponding height y, normalized by the reference height of y_0 (which is also equal to the boundary layer thickness $\delta = 0.99 * U_0$), to match the following power-law equation in **(2-1)**:

$$U = U_0 * \left(\frac{y}{y_0}\right)^{\alpha} \qquad \textit{(2-1)}$$

Figure 9a) shows that the two mean streamwise velocity profiles are well fitted with the 1/7 (0.14) power-law exponent α, which according to **Error! Not a valid bookmark self-reference.**, is the exposure category C for boundary layer thickness δ, of 27.4cm over a ground surface condition of an open terrain (ASCE 7-93). The atmospheric boundary-layer thickness for exposure category C differs from the simulated atmospheric boundary-layer thickness by approximately 5cm.

Table II: Values of z_0, D_0, α , and δ for Different Exposure Categories (Terrain Conditions) Used in ANSI A58.1-1982 and ANSI/ASCE-7-1988

Exposure Category	**Terrain Roughness z_0 (cm)**	**Surface Drag Coefficient D_0**	**Power-Law Exponent α**	**Atmospheric Boundary-Layer Thickness δ**	
				(ft)	**(m)**
A	80	0.0251	1/3	1500	457
B	20	0.0105	2/9	1200	366
C	3.5	0.0050	1/7	900	274
D	0.7	0.0030	1/10	700	213

Note: A = large cities, B = urban and suburb, C = open terrain, D = open coast.

The evaluated turbulent statistics, such as, the mean streamwise and vertical turbulence intensities profiles $Tu = \sqrt{\overline{u'(x,y)^2}/U_0}$ and $Tv=\sqrt{\overline{v'(x,y)^2}\,/U_0}$, expressed as a percent, are shown in Figure 9c) and d), respectively. Also, the Reynolds shear stress and turbulence kinetic energy plotted using the equations $RSS = \frac{-\overline{u'(x,y)v'(x,y)}}{U_0{}^2}$ and $K= \frac{1}{2}\left(\overline{u'^2(x,y)}+\overline{v'^2(x,y)}\right)$ are shown in Figure 9e) and f), respectively.

Conclusions from the atmospheric boundary layer simulation show that the fence models in the wind tunnel test section were submerged within a simulated boundary layer of about 22cm thick over an open flat terrain, resulting in a Reynolds number $Re = \frac{U_0{*}l}{\upsilon}$, of approximately $3.6\text{x}10^4$, based off the height of the fence for the characteristic length scale l, free-stream velocity U_0 of 5.53m/s and kinematic viscosity υ of air at 20°C. Therefore, the following PIV experimental tests of measuring the flow fields around the fence models were conducted with the oncoming wind speed setting of 5.53m/s.

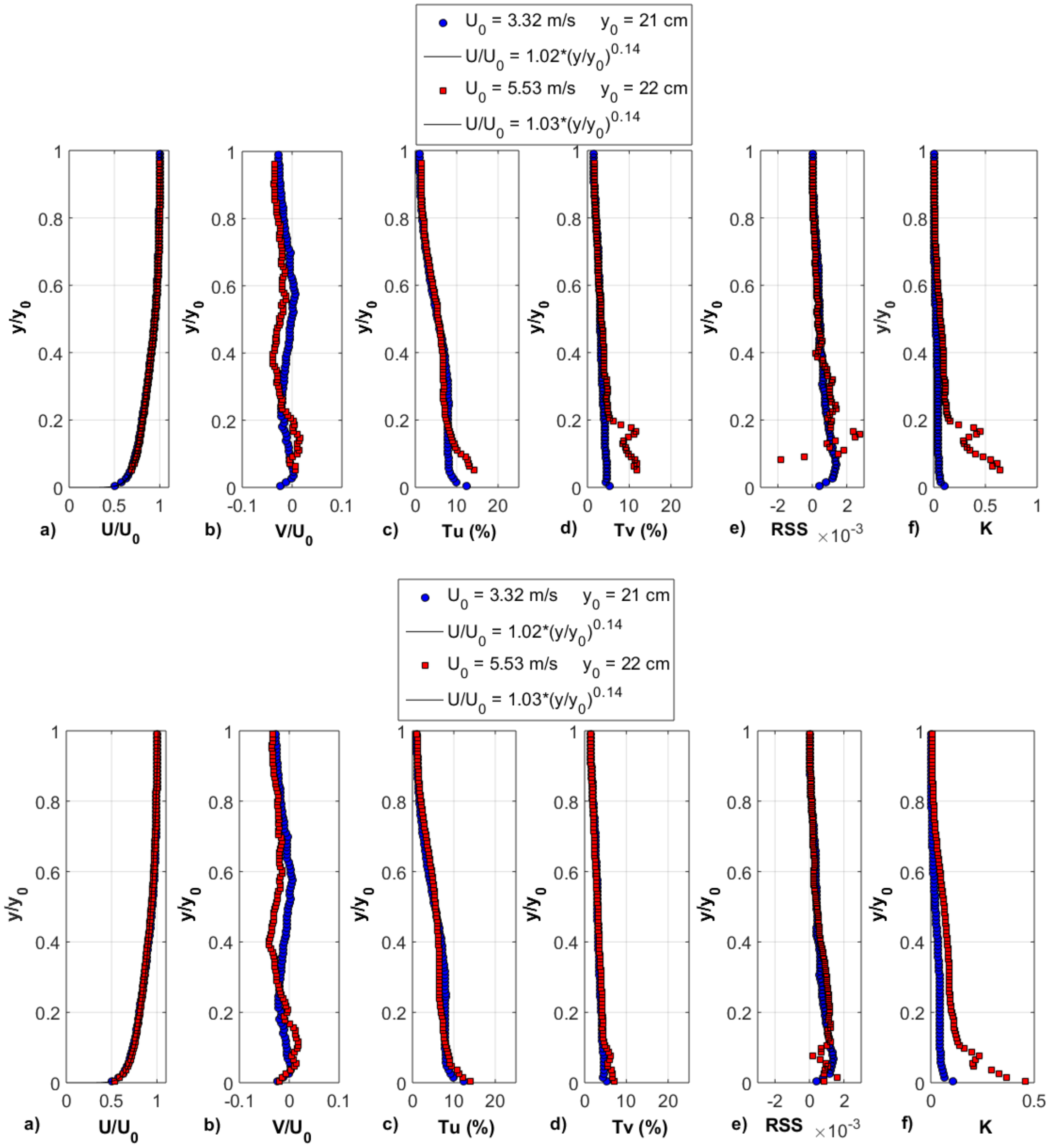

Figure 9: Vertical profiles of the ABL simulation: a) streamwise velocity, b) vertical velocity, c) streamwise turbulence intensity, d) vertical turbulence intensity, e) Reynolds shear stress and f) turbulence kinetic energy.

2.3. PIV experimental set-up

Experiments took place in the fully developed turbulent region of a closed-return type atmospheric boundary layer wind tunnel with test section dimensions of 6.75m x 0.72m x 0.48m (L x W x H) at the Biofluid and Biomimic Research Center at Pohang University of Science and Technology in South Korea shown in Figure 10. The systematic measurement technique using PIV measured whole velocity fields of the wind flow around the three fence models. The PIV experimental test plan captured the wind flow around the fence models from -0.5H to 7.5H in the x-direction and from 0H to 3.0H in the y-direction (with H meaning the height of the fence), illustrated in Figure 8b) and c). The laser light sheet for the measurement plane was set up along the centerline of the wind tunnel test section with respect to the spanwise (z - direction), parallel to oncoming flow. It was created by a combination of cylindrical lenses and deflected downwards by a 45 degree mirror. A schematic diagram of the experimental set-up and data acquisition system is shown in Figure 11.

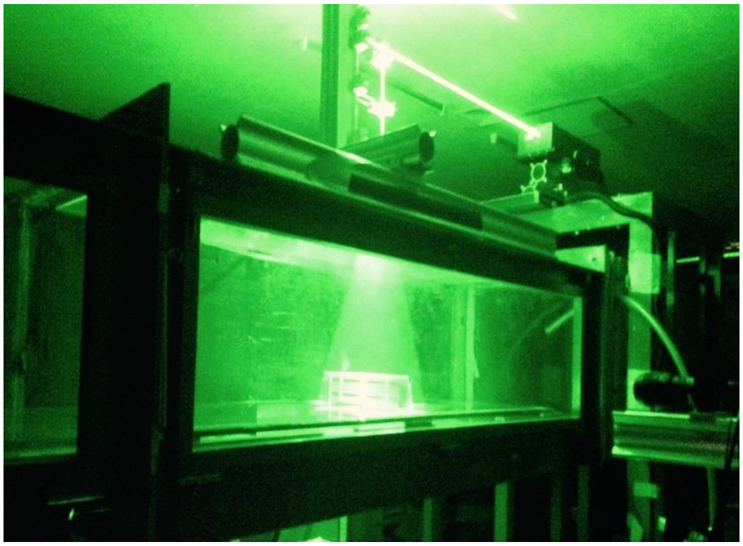

Figure 10: Picture of PIV test for flow around the 1D fractal fence model in the turbulent region of the atmospheric boundary layer wind tunnel at Pohang University of Science and Technology in South Korea

The PIV systematic measurement technique used olive oil tracer particles consisting of the same density as the wind flow and were seeded into the flow of the wind tunnel at the end of the 6.75m long test section. To illuminate the particles, a double-pulsed dual-head green light 532nm Nd: Yag Laser was used and captured the particles in the flow at a frame rate of 2.5 fps using a 4K x 4K CCD camera fitted with a 105mm focal lens optimized for 2D2C particle image velocimetry measurements which provided a spatial resolution of 4864(H) x 3248(V) pixels. This resulted in a maximum field of view of 49cm x 33cm. The double-pulsed laser and charged-coupled device (CCD) 8-bit camera were synced through a 565 Pulse/Delay Generator with a time interval dt, of 120 µs between laser pulses. In addition, the measurement planes for the three fence models were all approximately 60mm left-of-center from the centerline of each fence shown in Figure 12. Each measurement plane was adjusted slightly so the flow field was taken in between the fence struts and was not blocked by the fence structure. Furthermore, a total of 2400 samples (1200 pairs) of raw images were captured for each window (1 and 2) depicted in Figure 8b) and c), with

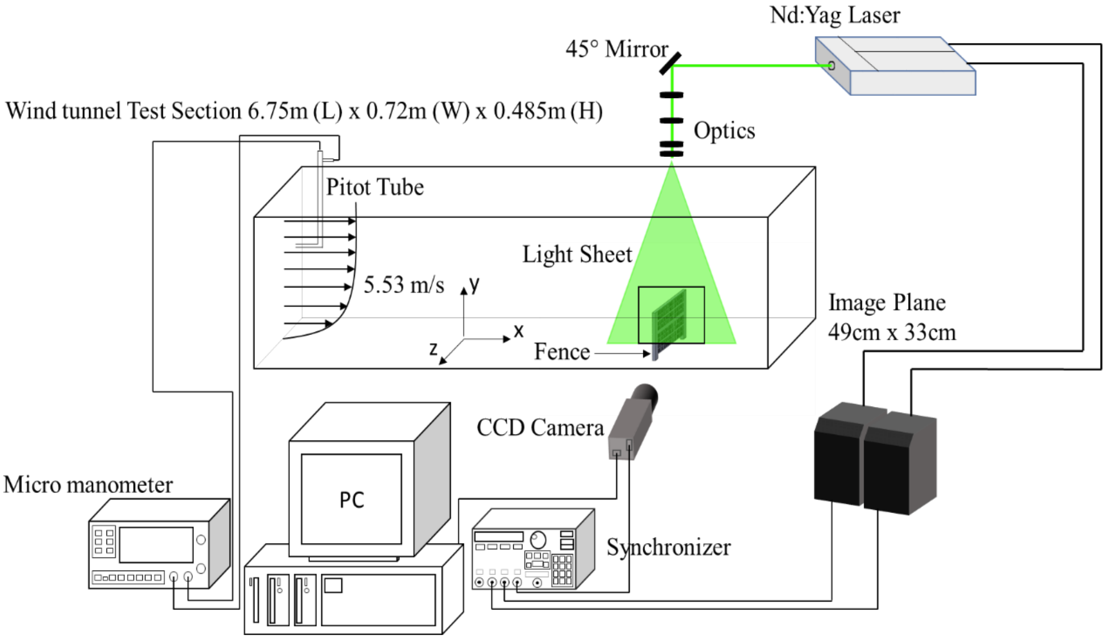

Figure 11: Schematic of experimental set-up

three hundred pairs of images taken in eight runs at a frame rate of 2.5 fps. The free-stream velocity was fixed at $U_0 = 5.53$ m/s, monitored by the micro-manometer, corresponding to a Reynolds number of approximately 3.6×10^4 based off the height of the fence.

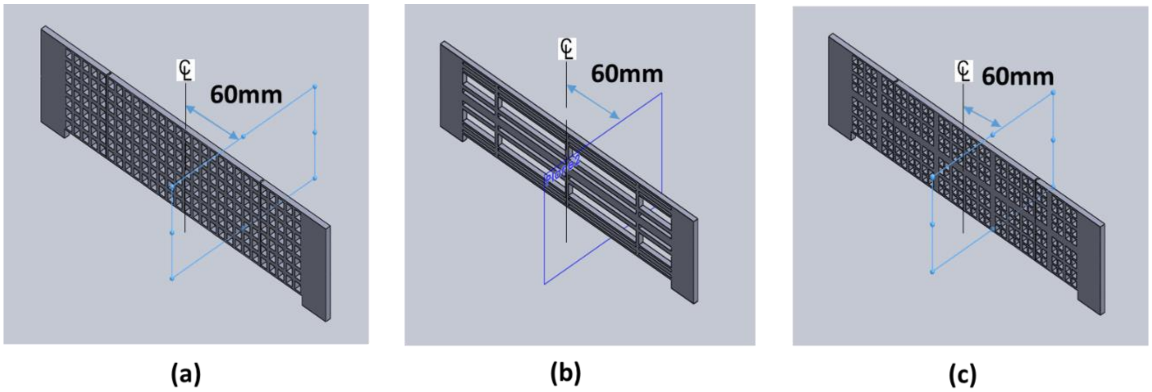

Figure 12: Measurement planes aproxmiately 60mm left-of-center for (a) conventional fence, (b) 1D fractal fence and (c) 2D fractal fence.

CHAPTER III

PIV DATA PROCESSING

3.1 PIV data processing

The PIV data processing procedure is illustrated in Figure 13: from a pair of raw particle images to an instantaneous velocity field for further analysis. First, an image pair- frame A and frame B, taken at time t with laser pulse 1 and then at time t+dt with laser pulse 2, respectively, is subdivided into interrogation windows or areas (IA) with typical window sizes of 64x64, 32x32 or 16x16 pixels. Although the IA can be as small as 4x4 pixels; however, a window size this small does not make much sense if a mean particle diameter is approximately 3pixels, because it is desired to have a presence of at least three or four particles to be matched within an IA (Raffel, Willert, and Kompenhans, 1998).

The second step of the data processing procedure is the selection of the correlation mode, which is applied to the two input interrogation windows I_1 and I_2, from the light exposure

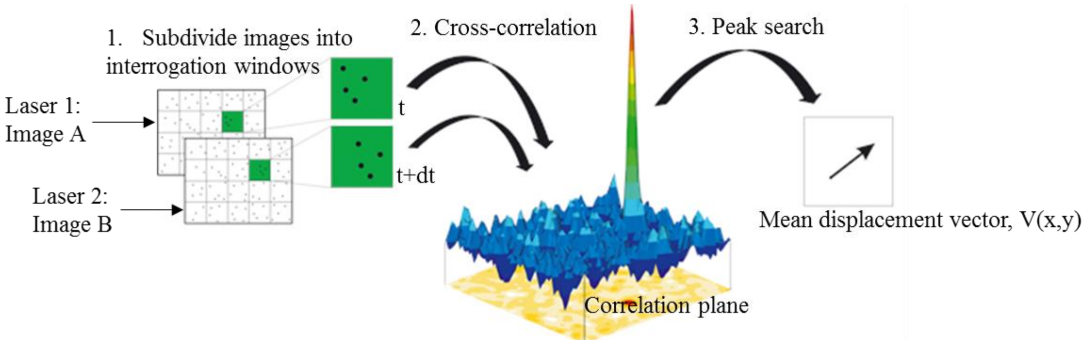

Figure 13: From a pair of raw particle images to an instantaneous velocity field for further analysis

at the two different times t and t+dt. The correlation plane for the size of an interrogation window at image position x, y is given by $C(x, y) = I_1(t, x, y) \otimes I_2(t+dt, x, y)$ (FlowMaster Product Manual, 2013). The correlation mode can be selected to be done in a single step or iteratively via multi-pass (constant or decreasing interrogation window size), amongst the selection of the interrogation window size and % overlap (used to shift the window in the second frame a certain percentage of the window size, as the particles shift to a different position in the second image, in order to match more particles for better peak detection).

Lastly, a peak detection of the highest correlation peak in the correlation plane is performed, whose position is representative of the mean displacement of the particle ensemble within the IA. The mean displacement vector V(x, y) at image position x, y is given by V(x, y) = position of highest peak detected in C(x, y) (FlowMaster Product Manual, 2013). The cross-correlation mode matches the particle shifts within each IA between the two frames, computing a single mean displacement vector simultaneously for each IA throughout the image, then combines all the vectors together to construct a 2D vector field for the whole image. An example of a resultant instantaneous vector field generated from the double-frame cross-correlation mode is shown in Figure 14.

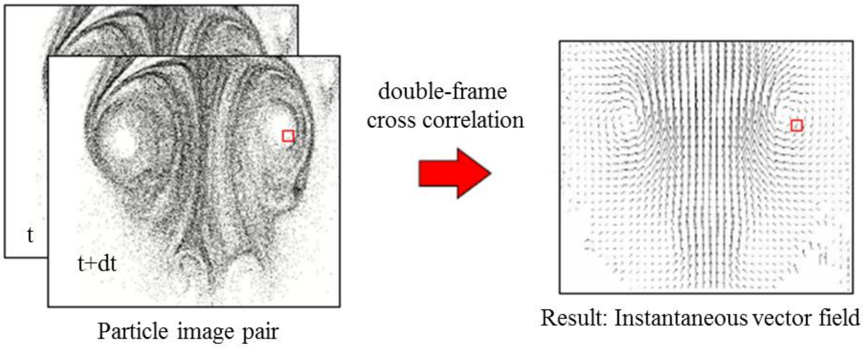

Figure 14: Construction of an instantaneous vector field from double-frame cross-correlation

3.2 Optimization of PIV processing

After acquiring the raw particle images and before the vector calculations are performed, the images may need to be optimized and manipulated by applying image pre-processing methods to improve the quality of the results. This was done using image pre-processing tools in LaVision's DaVis 8 software by experimenting several processing techniques such as background image subtraction and image masking. In addition, varying interrogation window sizes to compare correlation maps is performed to determine the optimal vector processing parameters. The following sections highlight the optimal parameters chosen in extracting the whole velocity field information for evaluation.

3.2.1 Background image subtraction

The purpose of subtracting the background image was to remove noise from the PIV images to enhance the particle illumination from the laser, in return to improve the quality of the results before applying an image correlation function (Honkanen and Nobach, 2005). A reference background image to be subtracted from the original images, can remove the local offset noise and intensity gradients from the laser light reflections off stationary objects (Honkanen and Nobach, 2005), and is commonly generated by computing an average or local minimum from all samples of a measurement set (Wereley et al., 2002). After subtraction of any background, it is desired that the images show only the illuminated particles in the flow and the object in which the flow is subjected to (which is later removed by image masking).

The concept for removing the average background is because of the random distributed particles captured in the image set from passing through the camera's field of view so quickly, will disappear when generating the averaged recording of all the images in the set, leaving only the background (Wereley et al., 2002). Then, the background can be removed from all raw images by subtracting all images in each set by the average background image generated. Although, reflections from stationary objects may not be removed in this manner because their brightness distributions do not change or move.

The concept for generating and removing the minimum background image described by Kühn, Kompenhans, and Monnier, (2000) follows that the pixels $M_{ijk}$of the two minimum images generated (one for image A and one for image B, hence *k=1,2*), consist of the ensemble minimum of the pixels P_{ijkn} of all the raw images in the set, and are calculated by $M_{ijk} = \min_n(P_{ijkn})$. Then, the two minimum images can be subtracted from all images in the set *n*, before evaluation by means of $P'_{ijkn} = P_{ijkn} - M_{ijk}$, for all *i, j* pixel positions in the domain. The removal of the minimum background at each pixel location is beneficial for reflections of stationary background objects because the minimum gray scale value at certain pixels within the domain may reflect the background brightness (Wereley et al., 2002).

The PIV images captured from the experiments exposed unwanted reflections of stationary background objects such as, ripples of black masking tape on the glass inside of the wind tunnel (on the opposite end of the glass closest to the camera), and reflections from part of the wind tunnel test section bed. The reflections revealed intensity gradients of the laser light off stationary object in the background of the images which may be interpolated as part of the particle intensities in the flow, causing erroneous vectors in the correlation analysis. Therefore, to remove this unwanted exposure of the background or offset noise from the images, the two primary background subtraction methods, subtracting the average and minimum background available in DaVis software were both tested.

First, the two methods were executed for only one set of 300 images (150 pairs) captured to see which subtraction method improved the quality of the images successfully before applying that technique to each set of 300 images (150 pairs) taken for each fence model. Figure 16 shows the result of subtracting the average background generated by averaging the 300 particle images in one set, comparing the raw image without background subtraction to its processed image with subtraction of the average background (right). The result of subtracting the average background was not adequate because reflections of the background were not fully removed. The reflections from the masking tape showed areas of even greater intensity rather than eliminating the reflections completely. Figure 15 shows the result of subtracting an image in the set by the minimum background image generated by the minimum pixel values in 150 images, comparing the raw image without background

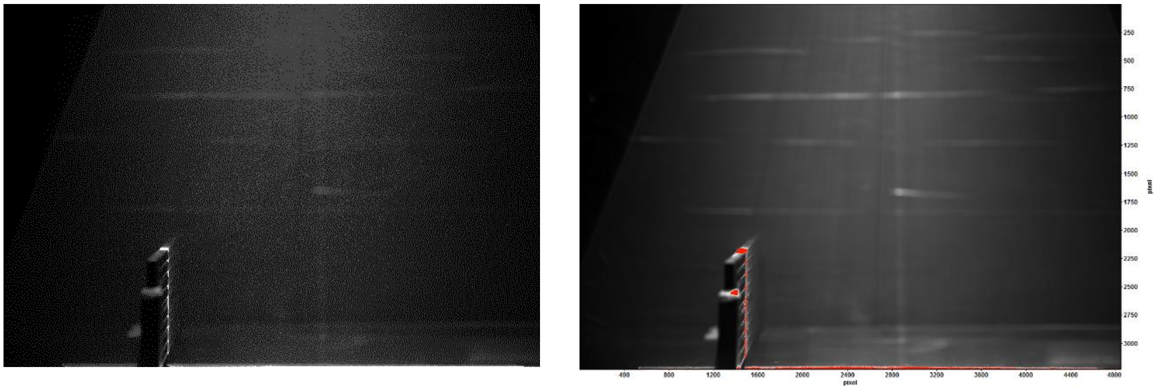

Figure 16: Original raw image (left) and subtraction of average background image generated by averaging 300 particle images (right)

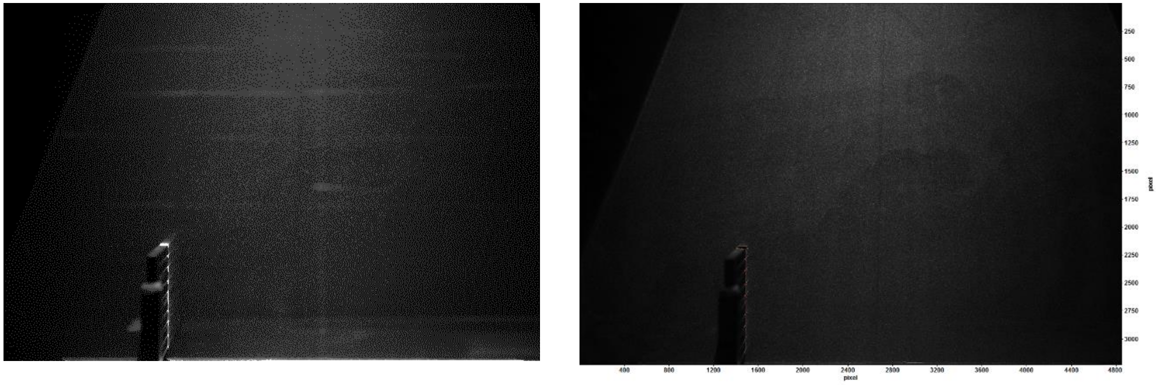

Figure 15: Original raw image (left) and subtraction of minimum background image generated by the minimum pixel values in 150 particle images (right)

subtraction P_{ijkn} (left) and the processed image with subtraction of the minimum background P'_{ijkn} (right). Subtracting the minimum background technique proved to work the best in removing the stationary objects because the reflections from the masking tape were fully removed and only the illuminated particles remained. Therefore, this image pre-processing technique of subtracting the minimum background was applied to every set of 300 raw images (150 pairs) acquired for each wind fence model experiment.

3.2.2 Mask for fence

Another image pre-processing technique used was to define a mask to remove the object that is subject to the flow in all the images by means of creating a geometrical mask. Points were selected to create lines around the model to mask out the fence to prevent erroneous vectors in the correlation analysis for the vector calculation. This simple technique after implementation the removal of subtracting the minimum background is shown in Figure 17.

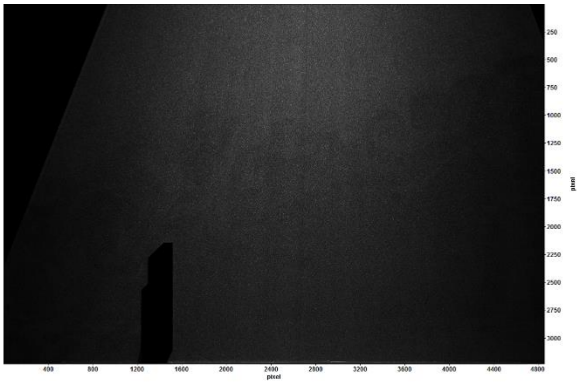

Figure 17: Processed image with minimum background subtraction and geometrical mask

3.2.3 Interrogation window size

A correlation peak detection was tested to ensure the right interrogation window size parameters were chosen for accuracy in the double frame cross correlation technique. It is important that the interrogation window size is not too small so enough particles (typically five) remain within the subdivided windows to determine the mean displacement. The maximum peak detected in the correlation plane indicates the mean displacement vector and the higher the maximum peak results in less false vectors. In addition, the wider the peak, the higher the uncertainty is in the measurements, (Xue et al., 2014).

A quick check for this parameter was to create a correlation map for each variation of interrogation window size at a specified location within a pair of images. Figure 18 shows the location in which the correlation maps were created from, shown in Figure 20, taken from the conventional fence data. The highest correlation peak was detected for an interrogation window size of 64x64 pixels in Figure 20 d) and the second highest detected was for 32x32 pixel window size in Figure 20 c). Figure 20 a) and b) for interrogation window sizes of 8x8 and 16x16 pixels show no distinguished peak and the width of the maximum peak is very large indicating not enough particles were correlated to determine an accurate mean displacement.

Given the particle image sets, selections for the vector calculation parameter among the multi-pass iteration options of either constant or decreasing interrogation window size, the minimum and maximum interrogation window sizes selected should be 32x32 pixels and 64x64 pixels, respectively. The effects of subdividing an image into interrogation window sizes of 64x64 pixels compared to 32x32 pixels, is that the amount of subdivisions is decreased by half, therefore resolving half the number of vectors throughout the domain. Consequently, it results in a reduced spatial resolution for the instantaneous vector field, which is a disadvantage.

Thus, shown in Figure 19 is a comparison of differences in interrogation window sizes for vector calculation parameters of (a) multi-pass (constant size) set to 64x64 pixels and (b) multi-grid refinement starting from 64x64 pixels to 32x32 pixels. Because a higher spatial resolution is desired to show better detail of the flow, the double-frame cross-correlation algorithm, with multi-grid refinement starting from an initial interrogation window size of 64x64 pixels down to 32x32 pixels with 50% overlap was chosen for the vector calculation parameter for all images.

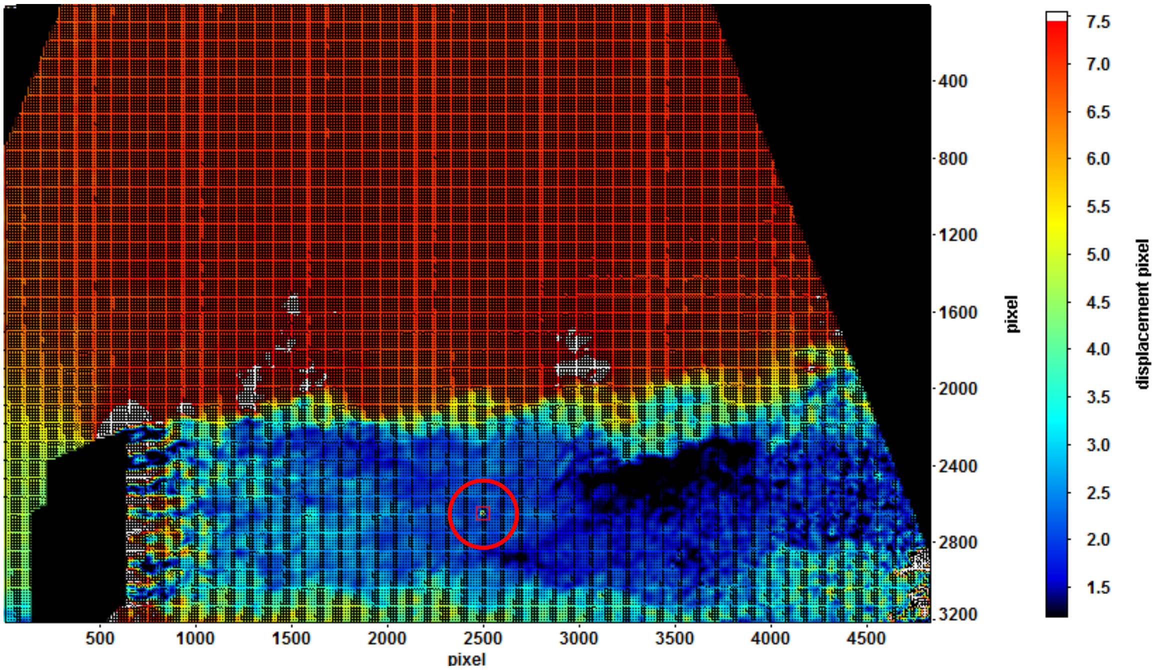

Figure 18: Location for interrogation window size correlation map

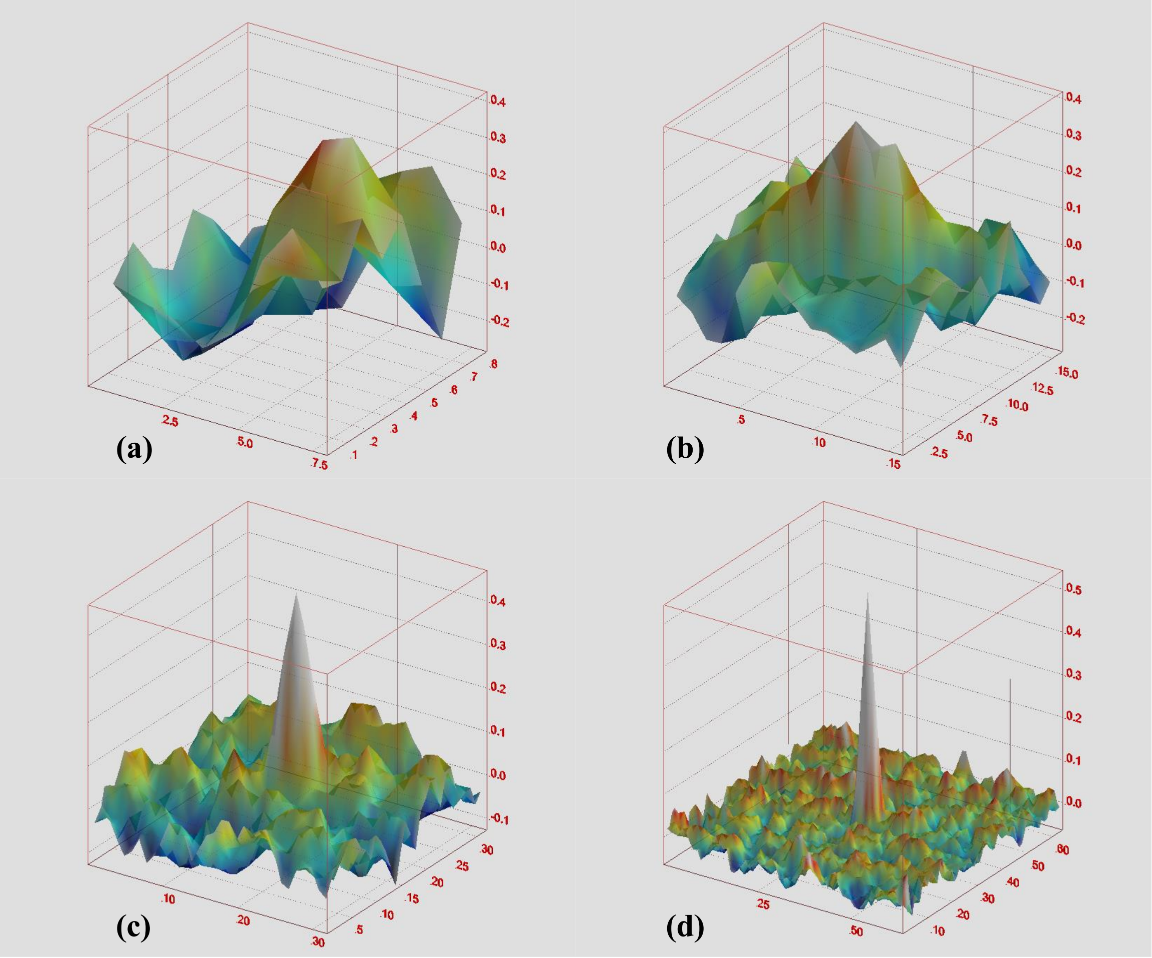

Figure 20: Correlation map for interrogation window sizes: (a) 8x8 (b) 16x16 (c) 32x32 and (d) 64x64 pixels

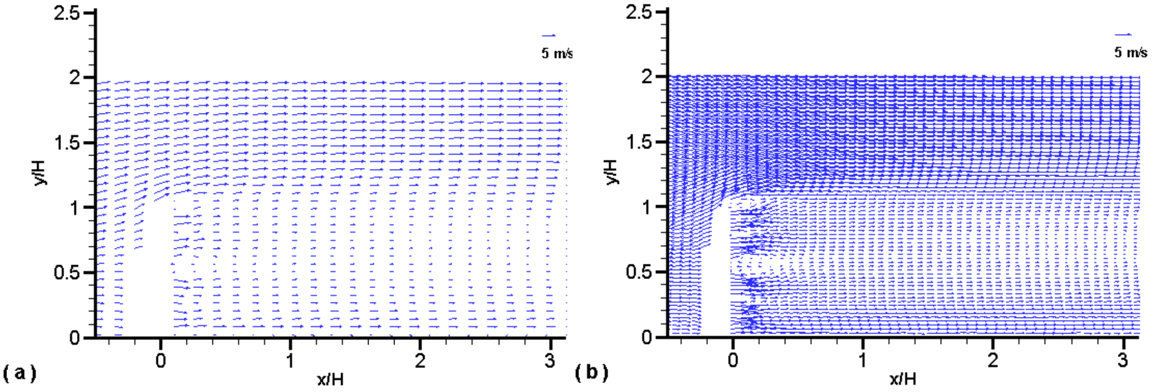

Figure 19: Comparison of instantaneous velocity field using (a) 64x64 pixels and (b) 32x32 pixels

3.3 PIV data analysis

After processing the raw particle images from each experiment, the instantaneous pixel-displacement vector fields were visually checked for outliers and removed. Then, the pixel-displacements were converted to velocity fields and ensemble-averaged, using a custom written MATLAB code. In addition, streamwise and vertical velocities and turbulent statistics such as, streamwise and vertical turbulence intensities, Reynolds shear stress, and turbulence kinetic energy were calculated. The MATLAB code created to perform these calculations is provided in Appendix B. The following sections outline the calculations used in the data processing stage to analyze the flow fields generated by the wind fence models.

3.3.1 Ensemble averaging procedure

Since the fence models were subject to a fully developed flow condition in the wind tunnel test section, the flow was considered steady opposed to drastically changing over time. In addition, each of the individual samples of the flow captured are considered random samples because of the low frequency laser causing a time restriction between each of the consecutive instantaneous vector fields captured, opposed to a continuously recorded collection of time series data. Therefore, the conventional averaging procedure for a statistically steady flow of discrete points (i.e., x, y), developed by Reynolds called ensemble averaging was used in order to determine the mean streamwise u, and vertical velocities v, (Anderson, et al., 2012). Thus, for any number of N samples of instantaneous velocity components $u_i(x,y)$ and $v_i(x,y)$, defined in the PIV experimental set-up Cartesian coordinates, in the horizontal and vertical planes, the ensemble-averaged velocities were calculated by equation **(3-1)** as follows,

$$\overline{u(x,y)} = \frac{1}{N}\sum_{1}^{N} u_i(x,y) \quad \text{and} \quad \overline{v(x,y)} = \frac{1}{N}\sum_{1}^{N} v_i(x,y) \qquad \textbf{\textit{(3-1)}}$$

The ensemble averaging was based on creating a cell array containing all instantaneous pixel-displacement fields from an experiment and averaging them by the total number of samples, using the mean function in MATLAB. After taking the mean of the pixel-displacement field data, the pixel displacements were converted to velocity vectors by multiplying pixel displacements by the number of pixels within 1cm (depicted from the scaling images taken after each experiment), and then dividing by the time interval, dt.

To investigate differences of the turbulent flow structure generated by each fence for the whole flow field, turbulent statistics were calculated by first splitting the instantaneous flow velocities into a mean and fluctuating part using Reynolds decomposition (White, 2011). The turbulent velocity fluctuations were determined by subtracting the mean flow from the instantaneous velocities in the domain for every flow field:

$$u_i'(x,y) = u_i(x,y) - \overline{u_\iota(x,y)} \quad and \quad v_i'(x,y) = v_i(x,y) - \overline{v_\iota(x,y)} \tag{3-2}$$

The root-mean-square of the turbulent fluctuations is also known as the standard deviation of the set of velocity fluctuations $u_i'(x,y)$ and $v_i'(x,y)$, (White, 2001).

$$u_{rms} = \sqrt{\frac{1}{N}\sum_1^N \left(u_i'(x,y)\right)^2} \quad and \quad v_{rms} = \sqrt{\frac{1}{N}\sum_1^N \left(v_i'(x,y)\right)^2} \tag{3-3}$$

Equation **(3-3)** corresponds to the strength of turbulence for the streamwise and vertical velocities u_{rms} and v_{rms}, respectively. Dividing the turbulence strength by the upstream velocity is the normalized turbulence intensity.

$$Tu = \frac{u_{rms}}{U_0} \quad and \quad Tv = \frac{v_{rms}}{U_0} \tag{3-4}$$

To evaluate the Reynold's or turbulent shear stress, the velocity fluctuations $u_i'(x,y)$ and $v_i'(x,y)$ were first found and then multiplied together for each instantaneous velocity field and afterwards time averaged and divided by the square of the oncoming flow speed, shown in **(3-5)**:

$$RSS = \frac{-\overline{u'(x,y)v'(x,y)}}{{U_0}^2} \tag{3-5}$$

For validation of the experimental measurements for numerical simulations, Reynolds shear stresses where $u_i(x,y) \neq v_i(x,y)$, are of importance because they impose changes in the flow and within a boundary layer they serve as the most dominant term in the non-linear Navier-Stokes equation which is known as turbulent shear (White, 2011).

The turbulence kinetic energy defined in **(3-6)**, is estimated using the two measured velocity components (White, 2011):

$$K = \frac{1}{2}\left(\overline{u'^2(x,y)} + \overline{v'^2(x,y)} \right) \qquad \textbf{\textit{(3-6)}}$$

3.3.2 Convergence test

For PIV measurements, it is imperative to collect an enough amount of samples to be ensemble-averaged to acquire true-mean flow field and turbulent statistics. This is important because the experimental accuracy is highly dependent on the total number of instantaneous velocity fields or sample size for ensemble averaging (Uzol and Camci, 2001).

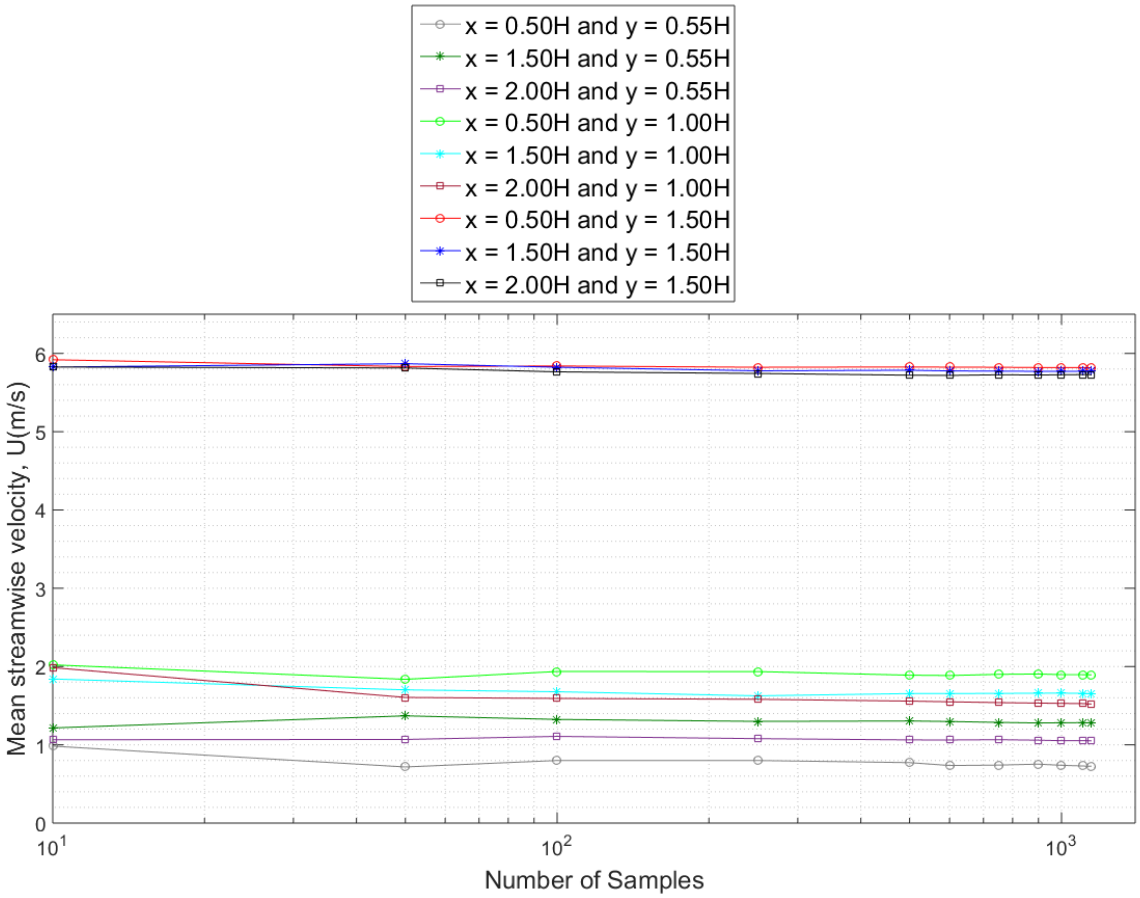

Figure 21: Mean streamwise velocity versus sample size

To check the convergence of the ensemble averaged PIV data for mean flow field statistics, variation of mean or averaged streamwise velocity with sample sizes of N = 10, 50, 100, 250, 500, 600, 750, 900, 1000, 1100, and 1147, is shown in Figure 21, for nine various locations within the 2D fractal fence domain clarified in Figure 25. Once reaching 250 samples, the averaged streamwise velocity is shown to converge. The total 1200 instantaneous velocity fields are able to ensure accuracy in the mean flow field statistics of the PIV measurements.

Similarly, to check convergence of the ensemble averaged PIV data for turbulence statistics, variation of mean or averaged streamwise turbulence intensity with sample sizes of N = 10, 50, 100, 250, 500, 600, 750, 900, 1000, 1100, and 1147, is shown in Figure 22, for the same nine locations of the 2D fractal fence domain. Once reaching 1000 samples, the averaged streamwise turbulence intensity is shown to converge. Again, the total 1200 instantaneous velocity fields are able to ensure accuracy in the turbulent statistics of the PIV measurements.

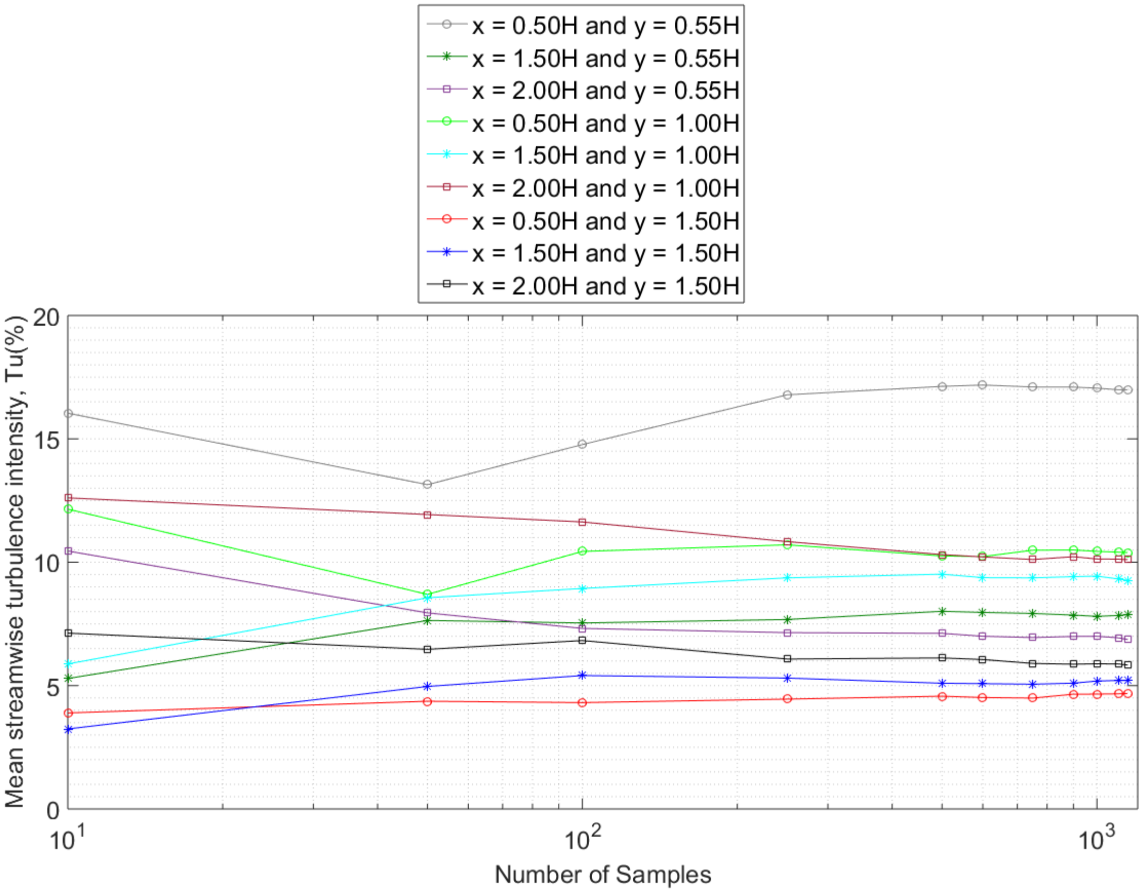

Figure 22: Mean streamwise turbulence intensity versus sample size

3.3.3 PIV uncertainty quantification from correlation statistics

In general, uncertainty (***u***) is an estimate of the range ($\pm \boldsymbol{u_d}$) within which we believe an actual value of an error (**δ**) lies. An error of a measurement is the difference between the measured value and the true value of the measurand. The probability that the true value lies within the uncertainty bounds is the confidence interval. An illustration of the estimated range of uncertainty and the error in measured data is shown in Figure 23.

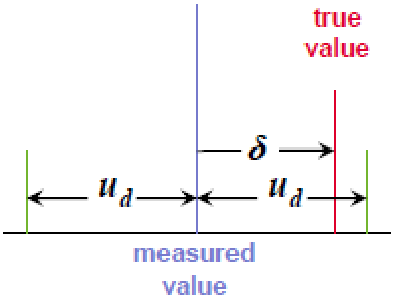

Figure 23: Uncertainty range and error (LaVision Inc.)

In the past years of PIV experimentation, people have reported rough estimates of uncertainties to be 0.1 or 0.05 pixel. In recent years attempts have been made to more accurately quantify the measurement uncertainty for a particular experimental setup and for every vector in the measured flow fields. Some of the newly derived methods are the ‘uncertainty surface’ (Timmins et al., 2012), the ‘peak ratio’ (Charonko and Vlachos, 2013), and the ‘image matching’ or ‘particle disparity’ method (Sciacchitano et al., 2013). An extension of the ‘particle disparity’ method which operates on a pixel level as opposed to analyzing particle positions, named the ‘correlation statistic’ method was used for this study in order to quantify an uncertainty for every vector in the measured velocity field (Wieneke, 2015). Although, some disadvantages of the method is its inability to detect outliers and bias errors (Wieneke, 2015).

The correlation statistics method derives an uncertainty estimation from overall pixel contribution fitted to the correlation peak shape (Wieneke, 2015). Illustrated in Figure 24, this method computes the standard deviations of the pixel-wise contributions of the particle intensity differences in each interrogation window of two images, and the expected asymmetry of the correlation peak. The method takes as input an image pair to be matched and the displacement field computed by the PIV algorithm.

First, the displacement field *u*(*x*) from a certain PIV algorithm, is used to dewarp back image 2 to overlay onto image 1 shown in Eqn.**(3-7)**. **Error! Reference source not found.**

$$I_2^*(x) = I_2(x + u) \tag{3-7}$$

where I_2 is the intensity function of the image 2. The correlation function C (u) for the computed displacement u, is defined by Eqn.**(3-8)Error! Reference source not found.**.

$$C(u) \;= \sum \big(I_1(x,y) I_2(x+u,y)\big) \;= \sum \big(I_1(x,y) I_2^*(x,y)\big) \tag{3-8}$$

Provided that the algorithm converged for an ideal noise-free image shown in Figure 24 (left), the correlated peak is symmetric, where $C_+ = C_-$.

Although, due to various error sources $I_1$and I_2^* will not match perfectly, as noise will be present and thus the correlation peak is non-symmetric, where $C_+ \neq C_-$, shown in Figure 24 (middle). The contribution of noise is the standard deviation of the changes in the correlation function $\Delta C = C_+ - C_- = \sum(I_1(x,y) I_2^*(x+\Delta x, y) - \sum I_1(x,y) I_2^*(x - \Delta x, y))$, shown in Eqn. **(3-9)Error! Reference source not found.**, and add up in a random walk fashion to a non-zero ΔC.

$$\sigma_{\Delta C} = \sqrt{\sum_{i=1}^{N} [C_+ - C_-]^2} \tag{3-9}$$

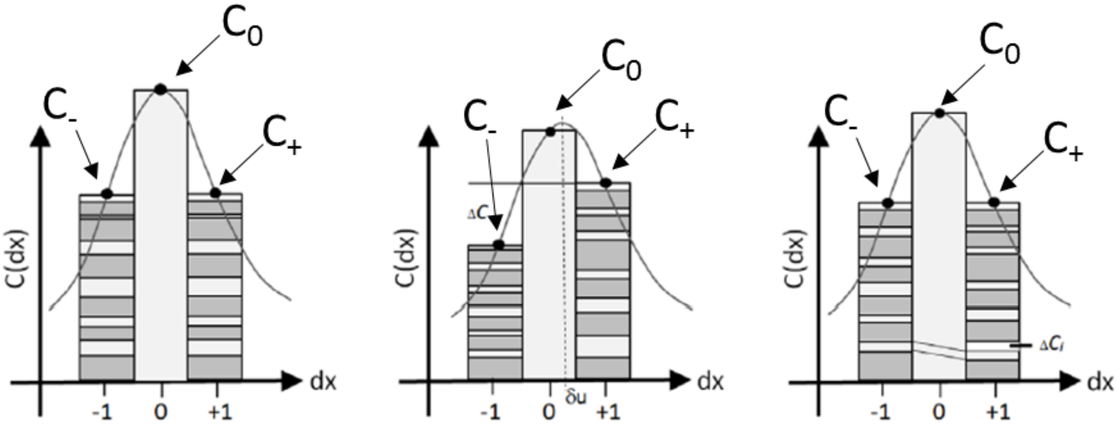

Figure 24: Correlation function between I_1 and I_2^* for ideal noise-free image (left). Compensating for noise, the correlation peak is non-symmetric (middle). Shifting the correlation peak back to 0, the measurement uncertainty is computed by a 3-point Gaussian fit (right).

Then, an optimal displacement δu is calculated by fitting the three points $C_0 = C\ (u)$, $C_+$and C_-, to a Gaussian curve performed by the PIV predictor-corrector scheme, such that ΔC is zero again, shown in Figure 24 (right), which leads to an erroneous measured displacement $u_{meas} = u_{true} + \delta u$. Then, with the given known variability in ΔC_i, an estimate for the standard deviation $\sigma_{\Delta C}$ of ΔC can be calculated and afterwards propagated by Eqn. **(3-10)** to compute an uncertainty estimation of the displacement field,**Error! Reference source not found.** with $C_\pm = (C_+ + C_-)/2$.

$$\sigma_u = f\left(C_0, C_\pm - \sigma_{\Delta C/2}, C_\pm + \sigma_{\Delta C/2}\right) \tag{3-10}$$

Davis software was used in order to quantify the total estimated PIV uncertainty calculated from correlation statistics $\sigma = \sqrt{\sigma_u^2 + \sigma_v^2}$. The measurement uncertainty was estimated and displayed in two ways for the 2D fractal fence model, providing an estimate for the whole flow field and locally for nine various points within the domain. The uncertainty estimates for the nine local points were tabulated for a 68% and 95% confidence interval and presented in Table III, of the results and discussion in section 4.1.2. The procedures to provide estimates of the uncertainty for the whole flow field and for the nine local points are further explained in the following.

The procedure to estimate the average and standard deviation of the uncertainty for the whole flow field is as follows:

1. within the processing tab of the Davis software (after selection of the post-processed instantaneous pixel-displacement vector fields), an additional component operation was calculated for the 'Uncertainty V';
2. within the export tab of the Davis software, the average and standard deviation of each whole uncertainty pixel displacement field was exported;
3. then, the uncertainty average and standard deviation for each instantaneous pixel-displacement vector fields were ensemble averaged and converted to velocity vectors in order to give an estimation of the uncertainty average and standard deviation in m/s, for the entire domain of the velocity field.

The second way to display estimates of uncertainty in the measurements and tabulate

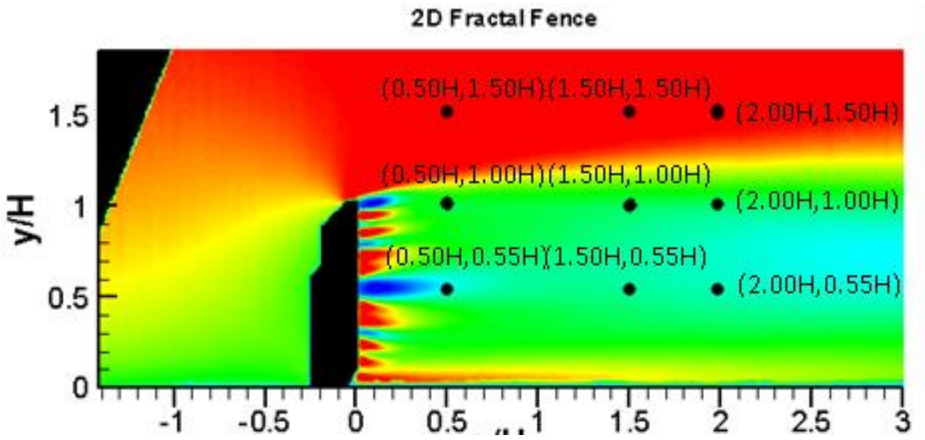

Figure 25: Nine locations for estimating uncertainty for the 2D fractal fence

for a 68% and 95% confidence interval, was too narrow in at nine various locations within the first window of the 2D multi-scale fractal fence domain, shown in Figure 25. The procedure to estimate the uncertainty in this manner is as follows:

1. The local average and standard deviation of the uncertainty estimates were depicted from the two plots in Figure 28 respectively, at the nine locations shown in Figure 25.
2. The values of the average uncertainty estimates depicted, were divided by two to be added and subtracted from the mean streamwise velocity measurements for each of the nine locations taken from the convergence plot in Figure 21, (i.e., (avg. uncertainty/2) ± (local converged streamwise velocity)).
3. To tabulate for a 68% confidence interval, the values of the standard deviation uncertainty estimates depicted, were divided by two and added and subtracted to the resulting value from (2) (i.e., (stdev. uncertainty/2) ± (avg. uncertainty/2) ± (local converged streamwise velocity)).
4. Two times the standard deviation widens the range of the uncertainty estimate and gives a 95% confidence interval for the estimated range in which the true value lies.

CHAPTER IV

RESULTS AND DISCUSSION

4.1 Evaluation of measurement quality

Plots were created to compare results of the mean flow properties and turbulence statistics normalized by the free stream velocity from this experimental study to other similar previous research works involving the study of porous non-fractal and fractal wind fence structures. The purpose of validating the measurements is to ensure they show some similarities with previous work done as well as for future experimental studies and comparisons to future numerical models.

4.1.1 Comparison to literature

A similar study of the structure of turbulent shear flow around a two-dimensional porous fence having a bottom gap (Kim and Lee, 2002) was used for graphical comparisons to be consistent with the conventional fence in this study having a bottom gap. The gap ratio of 0.1H is consistent with the gap ratio of this present study although, the porosity of the fence models between the two again differ. The 2D porous fence in Kim and Lee, (2002) had a porosity of 38.5% while the 2D conventional porous wind fence in this study has a porosity of 50%. However, there is shown to be better collapse of the data in comparison to the studies from Keylock, et al., (2012) and Lee and Kim, (1999), which are shown in

Appendix A in Figure 40 and Figure 41, respectively. Figure 26 and Figure 27 show vertical profiles along the fence height at different downstream locations from the fence of the normalized streamwise and vertical velocities and normalized streamwise and vertical turbulence intensities, respectively.

In Figure 26, the normalized streamwise and vertical velocities plots show similarities in shape up to $y/H = 1$. Above $y/H = 1$, the normalized velocities are higher in magnitude for the 38.5% porosity fence. The inconsistencies is due to the different experimental set-ups and inflow conditions. The experimental setup of Kim and Lee, (2002) used a circulating water channel where the boundary layer thickness is much smaller due to the density of water compared to the wind in the circulating wind-tunnel used for this study. In addition, the Reynolds numbers between the two experiments are quite different.

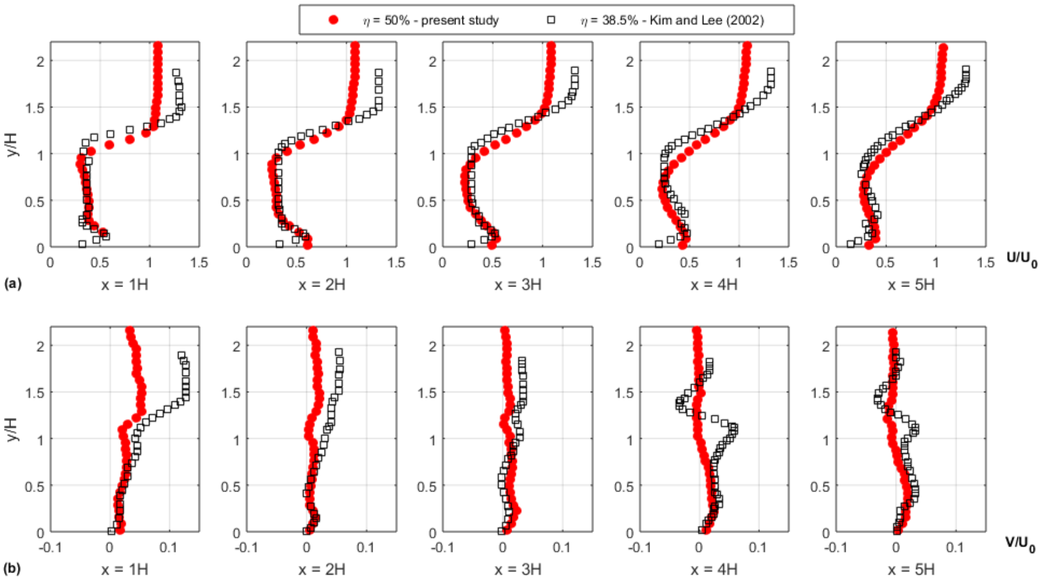

Figure 26: Comparison of two-dimensional (non-fractal) porous fences (a) normalized streamwise velocity and (b) normalized vertical velocity

Again, the vertical profiles in Figure 27 of the streamwise and vertical turbulence intensities are similar; however, the magnitudes of the intensities differ and increasingly worsen as the distance downstream increases. The magnitudes are higher for the 2D porous fence of 50% porosity when $0 \leq y/H \geq 1$ at locations $x \geq 3H$. Heisler, (1989) stated that in the lee of windbreaks the magnitude of the turbulent velocity fluctuations is inversely proportional to the porosity. In addition, Lee and Kim, (1999) compared laboratory measurements of the turbulent shear flow behind porous fences of different porosities and observed that as the fence porosity decreases, the fence wake has higher turbulence intensity. These conclusions are not seen in Figure 27, as the fence wake shows higher turbulence intensity for the 2D porous fence of 50% porosity.

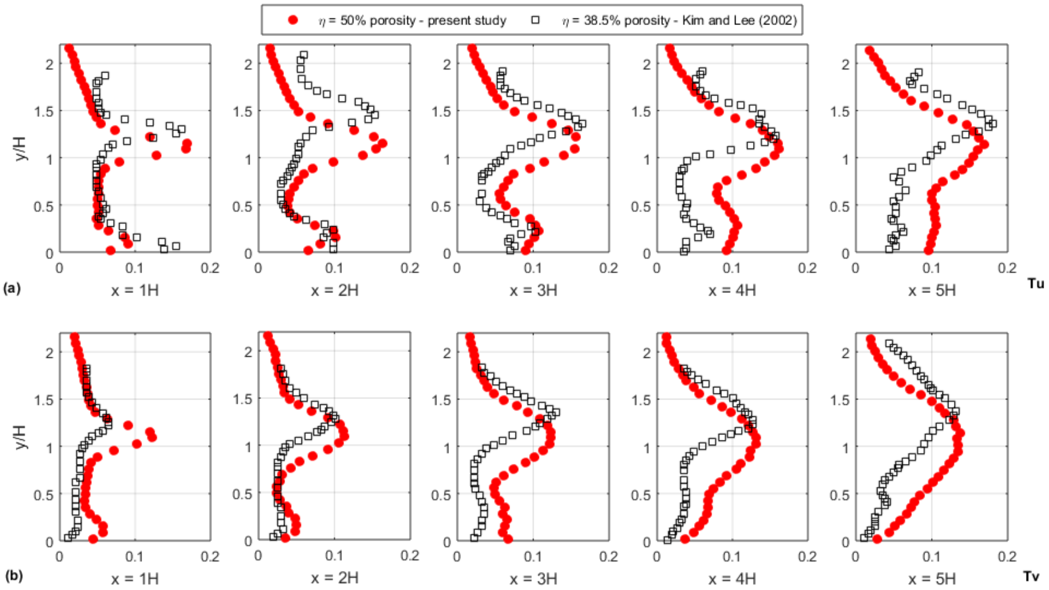

Figure 27: Comparison of two-dimensional (non-fractal) porous fences (a) normalized streamwise turbulence intensity and (b) normalized vertical turbulence intensity

4.1.2 Uncertainty

A typical total uncertainty field $\sigma = \sqrt{\sigma_u^2 + \sigma_v^2}$, with an average and standard deviation in pixels is provided to give an example of how to present an experiment uncertainty in conducting PIV measurements (Wieneke, 2015). The first procedure in section 3.3.3 highlights how to arrive at this result for this particular experiment. The uncertainty fields shown in Figure 28 are not uniform across the whole flow field. Wieneke, (2015) stated that even with perfect synthetic data, an uncertainty estimation field will show a variability in the uncertainty estimates between 5-25%. The average uncertainty field shown in Figure 28, displays a maximum average uncertainty estimation of approximately 35% of the oncoming flow speed of 5.53m/s. This maximum occurs at the edge of the laser light sheet near the ground surface at x/H > 3.1, where its intensity is the weakest. Fortunately, the data is overlapped and replaced by the second window as this was a known area that maximum uncertainty was predicted to occur. In addition, larger ranges of uncertainty occur at locations of high shear where the fluctuations in the flow are greater than in areas of low shear (Timmins, et al., 2012). Such regions in this experiment are within the shear layer produced by the increase of flow velocity over the top of the fence and in the near wake region of the flow through the fence holes where jets are formed.

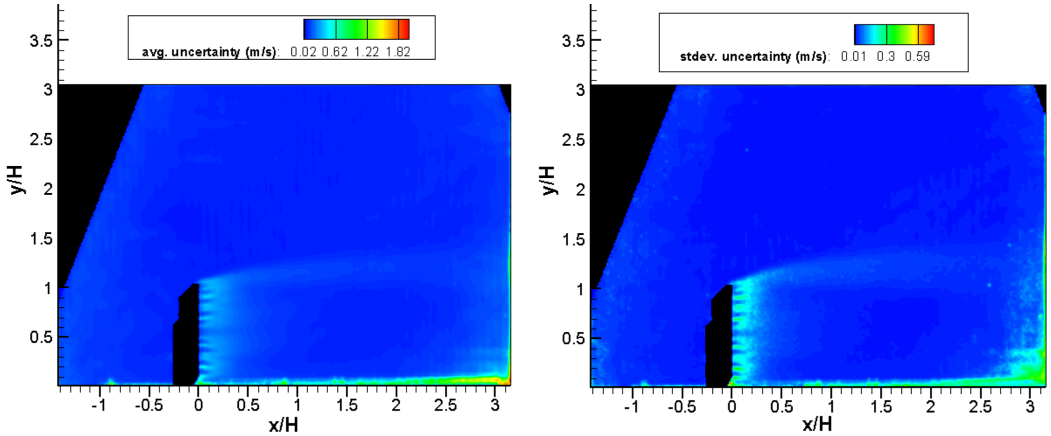

Figure 28: Average uncertainty field (left) and standard deviation uncertainty field (right).

Overall, the average estimated uncertainty for the whole velocity field of the first window of the 2D fractal fence is 0.136 pixel or 0.107 m/s (1.9% of the oncoming flow speed) with a standard deviation of 0.174 pixel or 0.137 m/s (2.5% of the oncoming flow speed). It has been validated by Monte-Carlo simulations that an accurate $\sigma_u \leq 0.3$ pixel (Wieneke, 2015), indicating the estimated uncertainty for this particular experiment is considered to be within an acceptable range, validating the measurements in providing a good estimate for the range in which the true value lies.

The second procedure in section 3.3.3 emphasized on the arrival for the uncertainty estimations for the nine locations within the domain of the 2D fractal fence shown in Figure 25. For the nine locations, the estimated range error of error in which the true value is predicted to lie within is given in Table III for a 68% and 95% confidence interval.

Table III: PIV measurement uncertainty for nine locations within the 2D fractal fence field domain.

Location		**Converged velocity**	**Estimated range of error**		**Estimated range of true value, U (m/s)**	
x	**y**	**U (m/s)**	**uncertainty (m/s)**	**standard deviation (m/s)**	**68% confidence**	**95% confidence**
0.50H	0.55H	0.726	±0.078	±0.027	(0.621-0.831)	(0.594-0.858)
0.50H	1.00H	1.894	±0.074	±0.024	(1.796-1.992)	(1.772-2.016)
0.50H	1.50H	5.817	±0.031	±0.009	(5.777-5.857)	(5.768-5.866)
1.50H	0.55H	1.28	±0.033	±0.008	(1.239-1.321)	(1.231-1.329)
1.50H	1.00H	1.654	±0.042	±0.014	(1.598-1.71)	(1.584-1.724)
1.50H	1.50H	5.771	±0.038	±0.012	(5.721-5.821)	(5.709-5.833)
2.00H	0.55H	1.052	±0.036	±0.010	(1.006-1.098)	(0.996-1.108)
2.00H	1.00H	1.521	±0.040	±0.015	(1.466-1.576)	(1.451-1.591)
2.00H	1.50H	5.729	±0.035	±0.012	(5.682-5.776)	(5.67-5.788)

The estimated uncertainty for the nine locations are even smaller than the average estimated uncertainty for the whole flow field, meaning that these local measurement uncertainty estimates are too within the acceptable range for validating accurate PIV measurement data representative of the true error for comparisons to possible future numerical model simulations.

4.2 Mean flow properties

The kinematic properties such as the mean streamwise and vertical velocities *U* and *V,* respectively were evaluated for each fence model up to 7.5H downstream and are shown in Figure 29. Unfortunately, due to the experimental limitations no more than 7.5H data downstream was able to be obtained. To zoom in on the differences in the near wake region, the mean streamwise and vertical velocities contour plots with streamlines up to 1H downstream are shown in Figure 30.

Common features of the streamwise and vertical velocities exist in the regions at the top of the fence, adjacent to the fence and at the bottom surface between all the fence models. However, in addition to these common features differences of the flow structure between the fence models are seen as well. The most common flow feature among all the fences is the incoming flow that speeds up as it approaches the fence. Higher magnitudes of the streamwise and vertical velocities are seen as the approaching flow speeds up over the top of the fence creating a shear layer between the outer flow and wake region. In addition, the wake that forms behind each of fences show similar flow features for both streamwise and vertical velocities. Although differences arise in the magnitudes of the flow among all the fences in the wake region. The greatest range of the streamwise velocity deficit is seen leeward of the 2D fractal fence between x = 1~5H with a maximum velocity reduction of 79% of the incoming flow speed occurring at approximately x = 3.6H. The range of the streamwise velocity deficit for the conventional fence is between x = 2.5~4H with a maximum velocity reduction of 76% of the incoming flow speed occurring at approximately x = 3H. The reduced velocity magnitudes leeward of the fence around these downstream locations are not seen by the 1D fractal due to the higher streamwise velocity magnitudes through from the larger openings of the fence structure compared to the 2D fractal and conventional fence.

Another common flow feature among all the fences in the near wake region adjacent to the fence, are the multiple jets of the flow blowing through the fence openings. However, the flow structure of the jets in the near wake are different for each of the fence models. The conventional fence shows more uniform jets while the fractal fences display symmetrical differences in the magnitudes of the jets formed at y = 0.55H, mid-height of the fence. Also, reverse flow occurs as well at mid-height of the fence for both the fractal fence models, which is more apparent in Figure 30. The reverse flow is caused by the higher magnitudes of the vertical velocities seen in the near wake for both the fractal fence models opposed to the conventional fence. The higher magnitude of the vertical velocities indicate stronger vertical motion which relates to enhanced mixing and therefore increased turbulence.

The last common feature among all the fence models is in the region near the bottom surface. Again, higher magnitudes are present here for both streamwise and vertical velocities. The higher velocity magnitudes corresponds to the increased flow through the bottom gap for all the fences. Although, the greatest magnitudes are seen near the ground surface of the conventional and 2D fractal fence, opposed to the 1D fractal fence.

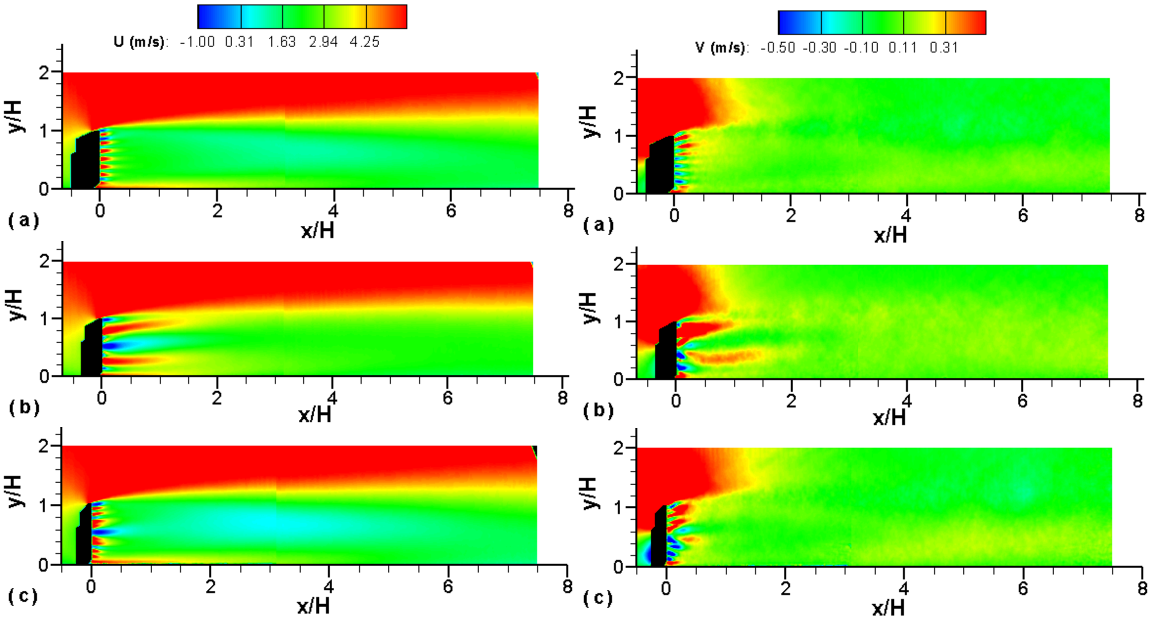

Figure 29: Mean streamwise velocity (left) and mean vertical velocity (right): (a) conventional fence, (b) 1D fractal fence and (c) 2D fractal fence

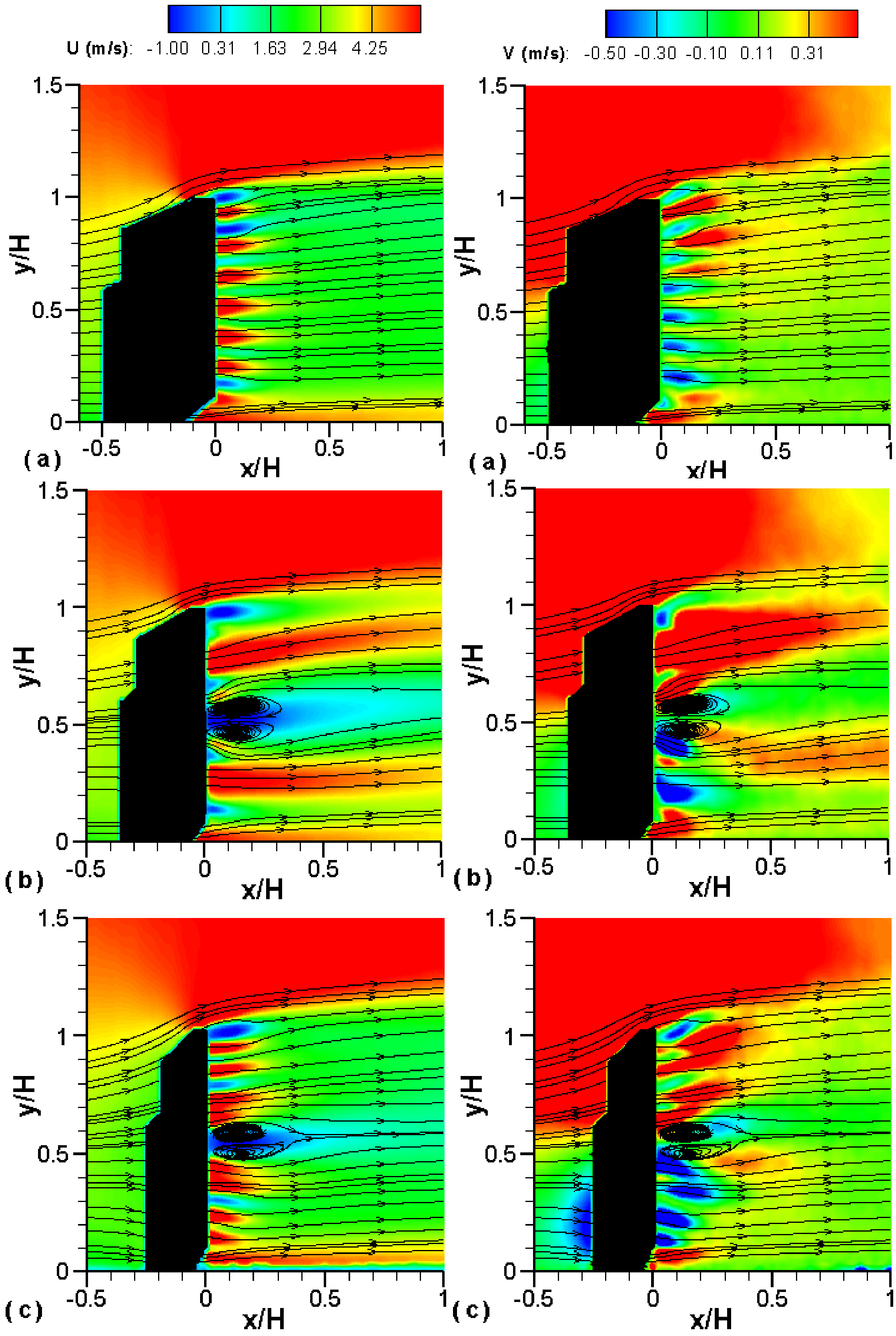

Figure 30: Streamlines of the mean streamwise velocity (left) and mean vertical velocity (right): (a) conventional fence, (b) 1D fractal fence and (c) 2D fractal fence

4.3. Turbulent statistics

4.3.1 Streamwise and vertical turbulence intensity

The normalized root-mean-square (r.m.s) streamwise and vertical turbulence intensity contour plots of the up to 7.5H leeward of the fence are given in Figure 31. Details of the streamwise and vertical turbulence structure in the near wake from 0H to 1H are shown in Figure 32. In the near wake region, the fractal fences generate an interesting symmetrical non-uniform turbulence structure caused by the fractal geometry, whereas the turbulence structure in the near wake region of the conventional fence is more uniform. The increase in turbulence seen by the fractal fences is related to the higher magnitudes of the vertical velocities compared to the conventional fence which is also indicative of enhanced mixing.

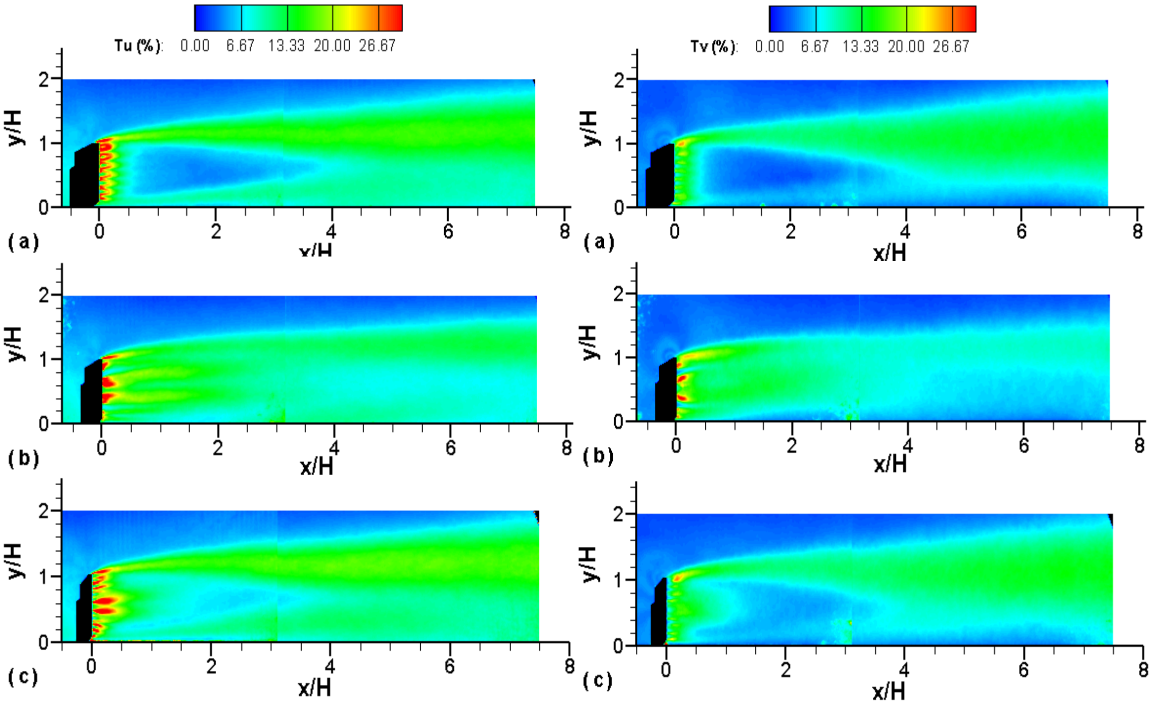

Figure 31: Streamwise turbulence intensity (left) and vertical turbulence intensity (right): a) conventional fence, b) 1D fractal fence and c) 2D fractal fence

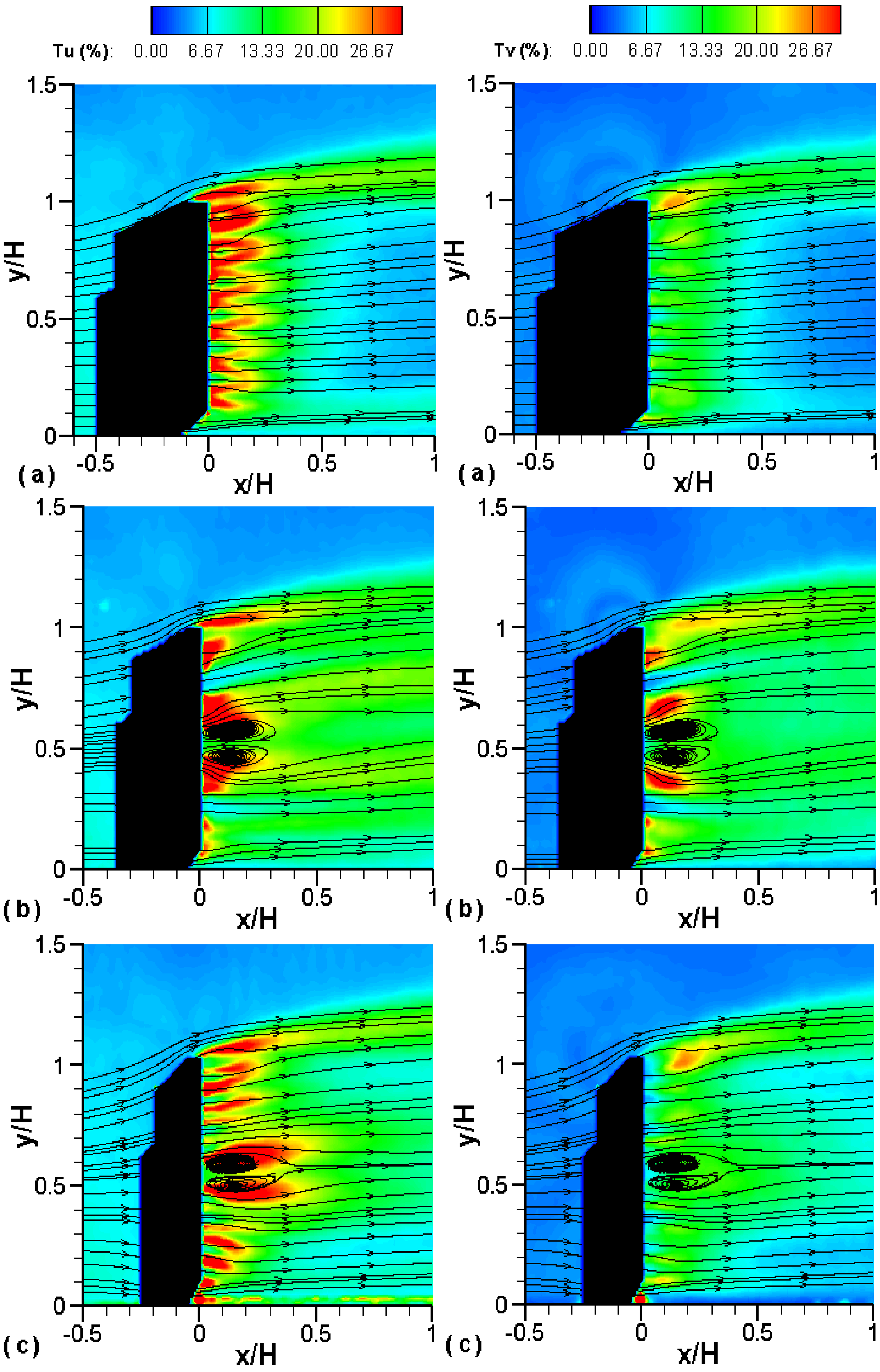

Figure 32: Near wake contour plots of the streamwise turbulence intensity (left) and vertical turbulence intensity (right): a) conventional fence, b) 1D fractal fence and c) 2D fractal fence

Among all of the fence models, in the near wake region the streamwise turbulence intensity levels are higher than the vertical turbulence intensity levels. The shortest range of the higher turbulence intensity levels that occur in the near wake region is from $0 \leq x/H \leq 0.2$ for the conventional fence. At $x/H > 0.5$, the intensities quickly dissipate. The turbulence intensities near the bottom surface from the opening of the bottom gap attach to the re-developing boundary layer at $x = 4H$, creating the triangular quiet zone consisting of the lowest levels of turbulence. For the 2D fractal fence, the greatest turbulence levels range from $0 \leq x/H \leq 0.5$ and significantly diminish when $x/H > 1.0$, about double the range of the higher turbulence levels in the near wake region of the conventional fence. In addition, similar to the conventional fence, the triangular quiet zone appears leeward of the 2D fractal fence from $1.0 < x/H \leq 4.0$. However, the quiet zone of the conventional fence is less turbulent compared to the 2D fractal fence due to the strut configurations between the two fences. The largest range and the highest turbulence levels occur in the near wake region for the 1D fractal fence from $0 \leq x/H \leq 4$. Then, the turbulence intensities start to dissipate to lower levels than the other two models as the distance downstream increases. This behavior is opposite of what is shown for the 2D fractal and conventional grid geometry as the distance downstream increases past 4H.

The maximum levels of the streamwise and vertical turbulence intensities in the absence of the fence, occur close to the ground surface of approximately 12% and 6%, respectively. Among the three fences, the level of the greatest streamwise turbulence intensity is 53%, generated by the 1D fractal fence adjacent to the fence in the near wake region at approximately $y = 0.42H$. The conventional and the 2D fractal fence generated the same amount of streamwise turbulent levels of approximately 49%, in the near wake region adjacent to the fence at y = 0.7H and 0.19H, respectively. The vertical turbulence intensities are about half of the magnitude of the streamwise turbulence intensities for all three fence models.

4.3.2 Reynolds shear stress

Another way to examine turbulence is through the Reynolds shear stress distributions shown in the plots of Figure 33. Wind fences exert a drag force on the flow and generate velocity gradients which cause shear layers to form. There are two common shear layers are present in Figure 33 for all three fence models, the thick positive upper shear layer starting at the top of the fence between the outer flow and wake region and the negative shear layer near the bottom surface formed between the quiet zone and the increased flow

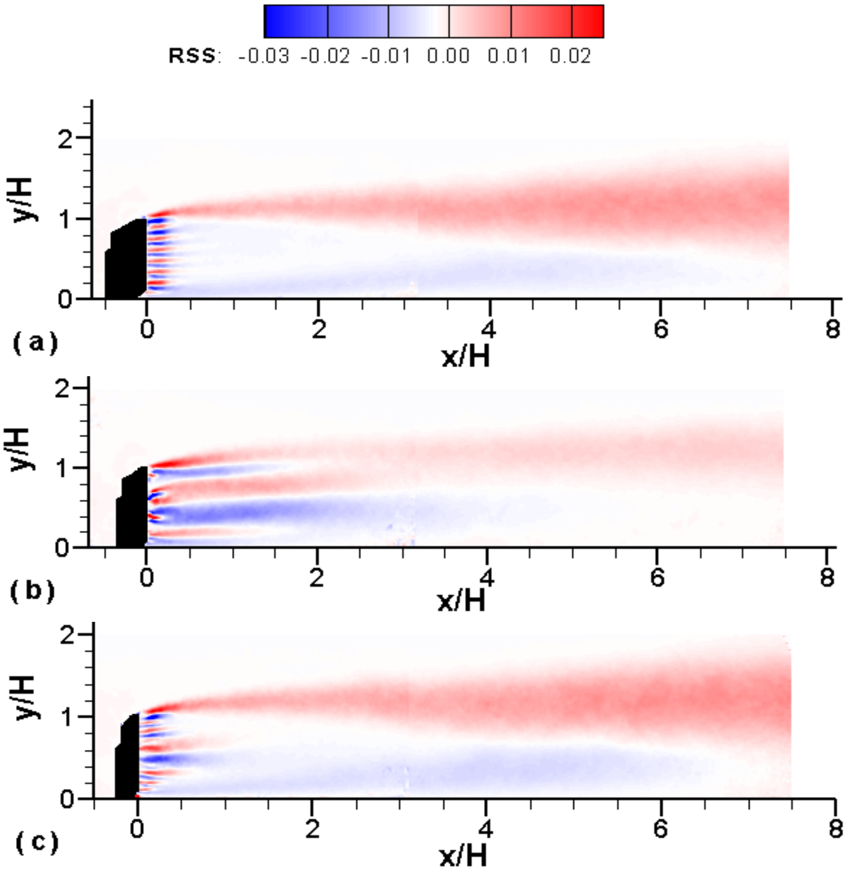

Figure 33: Reynolds shear stress: (a) conventional fence, (b) 1D fractal fence and (c) 2D fractal fence

through the bottom gap. Lowest values of RSS are present in the upper shear layer of the 1D fractal fence case compared to the other two fence models. In the near wake region each fence shows differences in smaller shear layers created between the blockage of the flow by the fence structure and the multiple jets blowing from the fence openings. The conventional fence shows uniqueness in the alternative high and low RSS zones having similar magnitudes normal to the fence plane. Higher values of RSS exist in the upper shear layer than in the lower shear layer, among the three fence models. Details of shear layers in the vicinity of the fence with streamlines are shown in Figure 34.

4.3.3 Turbulence kinetic energy

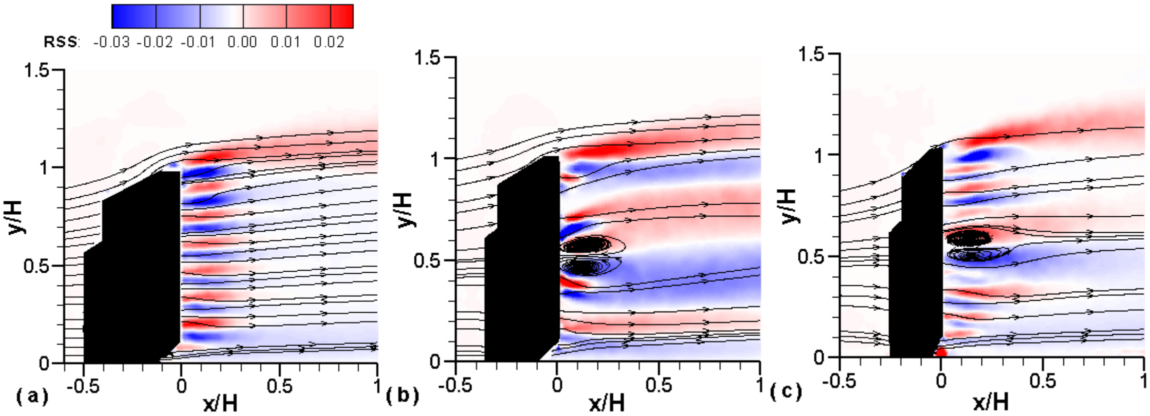

Figure 34: Reynolds shear stress with streamlines: (a) conventional fence, (b) 1D fractal fence and (c) 2D fractal fence

Turbulent shear stresses impose changes in the flow and are directly related to the turbulence kinetic energies of the flow. Therefore, the areas of increased turbulent shear stresses correlate to the areas of greater turbulence kinetic energies. The turbulence kinetic energies were evaluated to compare the energies in the turbulent velocity fluctuations of the flow fields past the three wind fence models up to 7.5H downstream shown in Figure 35. Among the three wind fence models, the greatest magnitudes of the turbulence kinetic energy exist farther downstream from x = 4H to 7.5H for the 2D fractal fence with the lowest magnitudes occurring in this area for the 1D fractal. This is due to the higher magnitudes of the vertical velocity fluctuations downstream of the 2D fractal fence compared to the other two fence models. However, the greatest magnitudes of the turbulence kinetic energy exist in the near wake region from x = 0H to 2H for the 1D fractal fence with the lowest magnitudes occurring in this area for the conventional fence. As it is preferable to prevent particle remobilization from excessive turbulent stresses during an event of snow fall, the lower kinetic energy magnitudes generated by the 1D fractal are more desirable farther downstream. Although, the lower kinetic energy magnitudes in the wake region from x = 0.5H to 4H of the conventional fence are better than the energies in this region for the other fences. Depending on the purpose for the wind fence, future studies can resort to these conclusions in designing a more efficient wind fence to suit their needs.

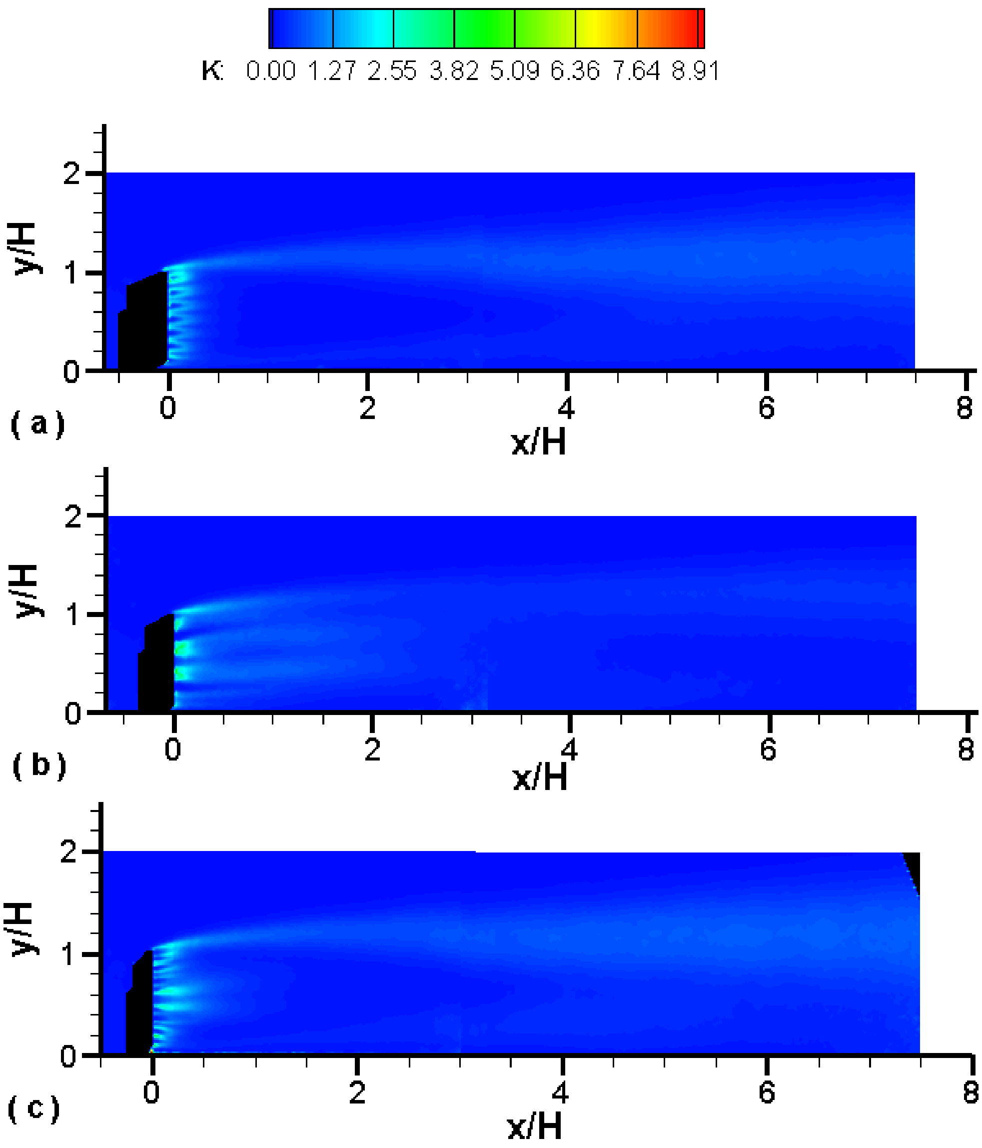

Figure 35: Turbulence kinetic energy: (a) conventional fence, (b) 1D fractal fence and (c) 2D fractal fence

4.4 Wind-speed reduction coefficient

One of the parameters used to evaluate the effectiveness of wind fences is the wind-speed reduction coefficient. To provide a quantitative comparison of the effectiveness of each model to reduce the incoming wind velocity at a given height above the surface and distance downstream, the wind-speed reduction coefficient proposed by Cornelis and

Gabriels (2005) was calculated. The dimensionless reduction coefficient is stated in Eqn. **(4-1)**.

$$Rc_{\Delta x,y}=1-\frac{u_{\Delta x,y}}{u_{0_{\Delta x,y}}} \tag{4-1}$$

where Δx is the distance either windward or leeward of the fence in terms of fence height H, Δy is the height above the ground surface, $u_{\Delta x,y}$ is the time-averaged wind speed past the fence and $u_{0_{\Delta x,y}}$ is the time-averaged wind speed in the absence of the fence (Cornelis and Gabriels, 2005). A magnitude of 1 for $Rc_{\Delta x,y}$ suggests that the fence is 100% effective in complete reduction of the incoming flow, denoting zero velocity leeward of the fence along the fence height.

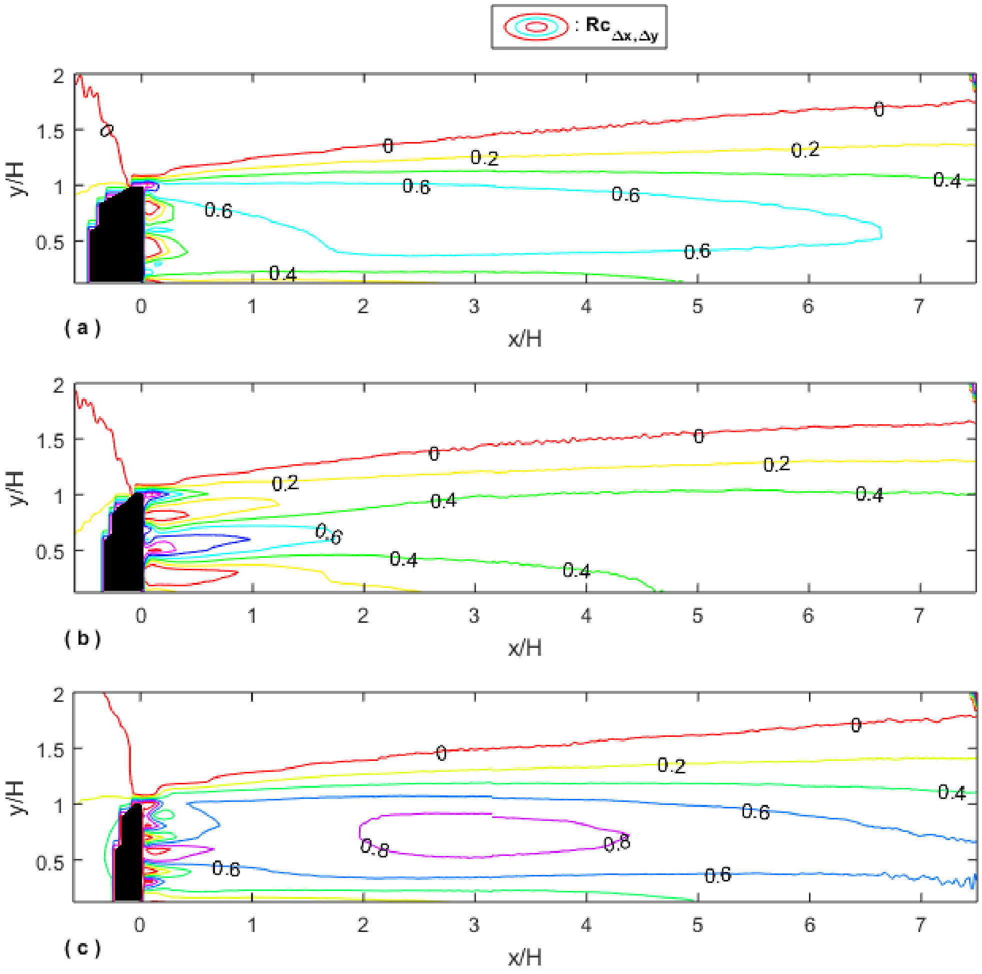

Figure 36: Wind-speed reduction coefficient for (a) Conventional fence, (b) 1D fractal fence and (c) 2D fractal fence

A contour plot showing the comparison of the wind-speed reduction coefficient up to 7.5H downstream for the three fence models is shown in Figure 36. The formation of the contours for the conventional fence are similar to that of the 2D fractal fence; however, the 2D fractal reveals a larger wind-speed reduction coefficient achieving a magnitude of 0.8 from approximately 2H to 4.5H downstream of the fence. In addition, larger coefficients extend farther downstream past 6.5H, for the 2D fractal opposed to the conventional fence. The 1D fractal only displays high magnitudes in the near wake region up to x~2H. Conclusions of this parameter graphically show the 2D fractal fence is more effective in reducing the wind-speed not only farther downstream but to a greater extent.

Lee, et al., (2014) study on the shelter effect of a fir tree with different porosities was used to match the similarities between natural and artificial fractals as windbreaks. Consequently, trees which are very effective natural windbreaks as well as fractals in nature, comparisons in the magnitude of the wind speed reduction coefficients were plotted against the 1D and 2D multi-scale fractal fences implemented in this study. The wind-speed reduction coefficients of the control and leafless tree conditions of 30% porosity and 90% porosity, respectively in Leet, et al., (2014) were re-plotted against the 1D and 2D fractal fences of 50% porosity, to only show data up to 7.5H downstream to be consistent with the extent of data available in this study, shown in Figure 37. Due to the differences in the porosities of the tree models used by Lee, et al., (2014) to that of the fractal fence models in this study, the profiles of the wind-speed reduction coefficient show no distinct correlations.

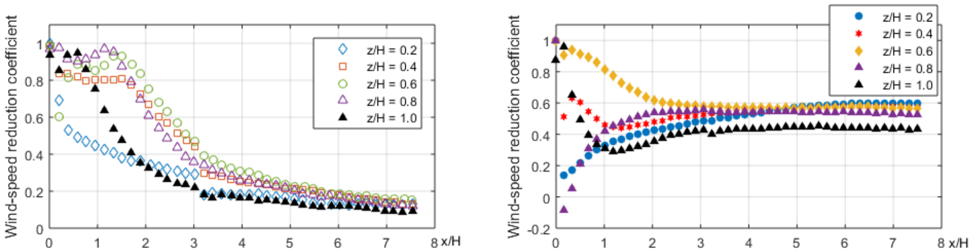

(a) Control condition η = 30%

(c) 1D Fractal η =50%

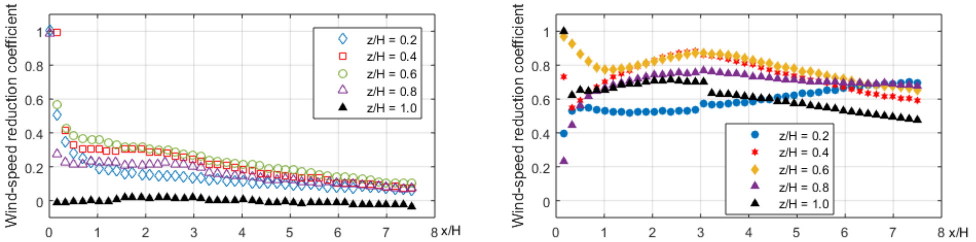

(b) Leafless condition η = 90%

(d) 2D Fractal η = 50%

Figure 37: Wind-speed reduction coefficient comparison of natural (tree) to artificial (1D/2D fence models) fractal windbreaks

In addition, the three fence models in this study were plotted together to observe comparisons in $Rc_{\Delta x,y}$ for the 2D conventional (non-fractal) porous fence to that of the two fractal porous fence models, shown in Figure 38. Again, among the three fence models in this study, the 2D fractal and conventional fence show similar profiles in $Rc_{\Delta x,y}$, such that at approximately 3H downstream the maximum reduction in wind speed occurs and then starts to decrease. A benefit to graphically showing horizontals profiles of $Rc_{\Delta x,y}$ at different heights compared to the contour plots, is that the maximum magnitude of the coefficient achieved is exposed. The 2D fractal fence reveals a maximum coefficient of approximately 0.9 at about x = 3H, which is slightly higher than previously stated. Moreover, the 1D fractal reaches a maximum in the near wake region at approximately x = 0.5H and then quickly levels off approaching a coefficient of 0.4, as the distance downstream increases. In addition, the range of coefficients is narrowed from the ground surface to the height of the fence at 7.5H for the 1D fractal opposed to the conventional and 2D fractal.

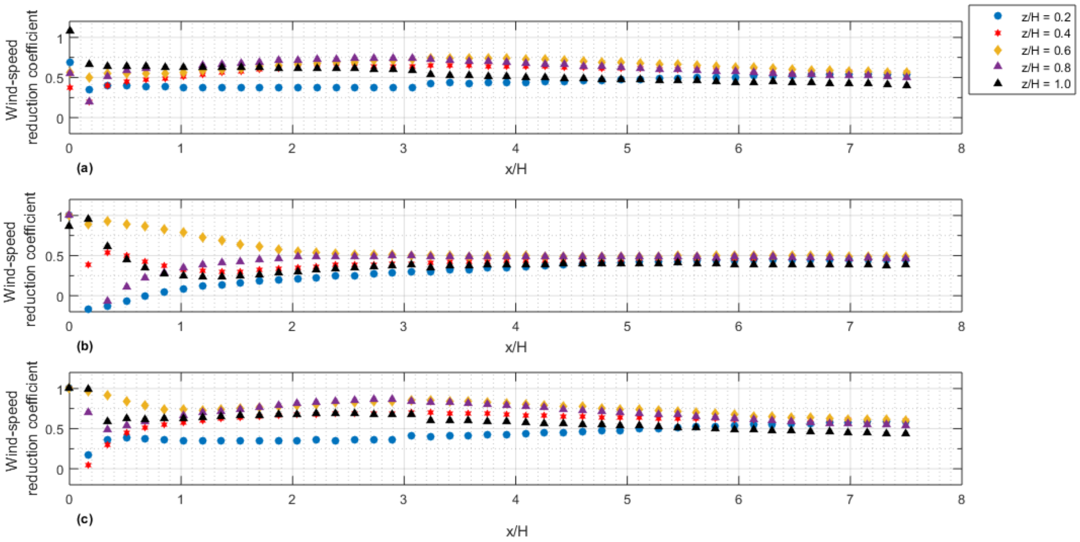

Figure 38: Wind-speed reduction coefficient for (a) conventional fence, (b) 1D fractal fence and (c) 2D fractal fence

4.5 Shelter effect

Another common parameter used to determine the effectiveness of wind fences is the shelter effect. To analyze the shelter effect of the three fence models, the modified version proposed by Kim and Lee, (2002) based off previous versions was implemented. Contour plots of the shelter parameter for all three fence models are shown in Figure 39. This modified shelter parameter is believed to be more accurate as it incorporates both the streamwise and vertical velocity components and their standard deviations for the disturbed flow over the streamwise velocity and its standard deviations of the undistributed flow. The shelter parameter proposed by Kim and Lee is given in **(4-2)**.

$$\psi = \frac{|U| + \sigma(u) + |V| + \sigma(v)}{U_0 + \sigma\,(u_0)} \tag{4-2}$$

The vertical velocity and vertical standard deviations of the undisturbed flow are not considered in the parameter unlike versions of the shelter effect in previous studies because the undisturbed flow should have very little and thus negligible vertical velocity and fluctuations because of the constant wind speed and uniformity of the flow in the wind-tunnel. As the main purpose of a wind fence is to maximize the reduction of oncoming flow velocities, a lower value for the shelter effect parameter is desirable.

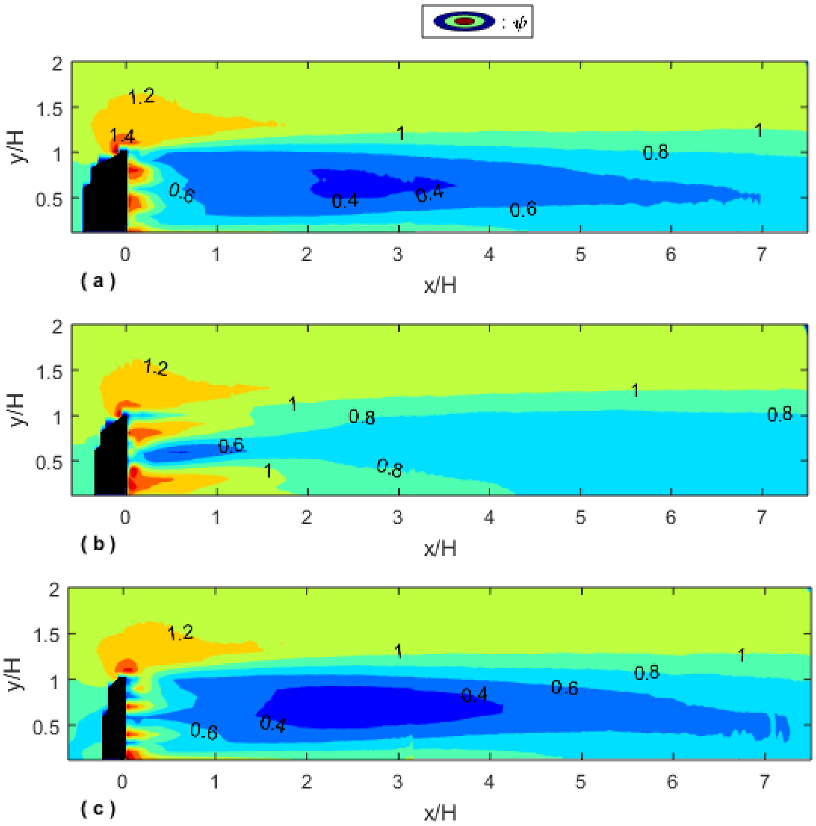

Figure 39: Shelter effect for (a) conventional, (b) 1D fractal and (c) 2D fractal fence.

The conventional fence and the 2D fractal fence have similar shelter effect parameter distributions; however, the 2D fractal has a longer area of shelter corresponding to the magnitude of 0.40, which is a good shelter effect. The range of this degree of shelter expands from x = 1.5H ~ 4.5H downstream of the 2D fractal fence, whereas the range for the conventional fence is only from x = 2.0H ~ 3.5H. The length of the 2D fractal fence shelter zone almost doubles from the conventional grid fence geometry. The 1D fractal experiences a medium shelter zone and does not reach magnitudes of the degree of shelter compared to the conventional or 2D fractal fence. The difference is due to the distribution of the voids in the 1D fractal geometry allowing greater quanities of the approaching flow through the larger open areas, even though each of the fence models have the same porosity.

CHAPTER V

CONCLUDING REMARKS

To explore the effectiveness of multi-scale fractal wind fences, in this study an experimental investigation of the turbulent flow around 1D and 2D multi-scale fractal wind fences was conducted in an atmospheric boundary layer wind tunnel. Velocity fields around the two fractal fences were systematically measured using 2D2C PIV at the Reynolds number of approximately 3.6x10^4 based on the free-stream speed and the fence height. Mean flow properties such as streamwise and vertical velocities were obtained from the ensemble-averaged measured flow fields. The fluctuating velocities were used to calculate turbulent statistics including turbulence intensities, Reynolds shear stress $[-\frac{\overline{u'v'}}{U_0^2}]$ and turbulence kinetic energy. The turbulent flow structures induced by specific 1D/2D multi-scale fractal wind fences were compared to those of a conventional grid fence of the same porosity (50%). Furthermore, wind-speed reduction and shelter effect parameters were evaluated to determine the effectiveness of the wind fences.

The major findings of this research show the 2D fractal fence is the most effective in reducing the wind-speed, showing an impressive wind-speed reduction coefficient of 0.9, and also displays a remarkable sheltering effect of 0.4 leeward of the fence from x = 1.5H to 4.5H, among the three wind fences. However, near the surface, the Reynolds shear stresses are very high for the conventional and 2D fractal fence, which is an indicator of potential particle remobilization. In contrast, the 1D fractal fence has the lowest Reynolds shear stress near the surface, which suggests the 1D fractal fence may be better in preventing particle remobilization from excessive turbulent stresses. Overall, it is desired for the design of wind fences to reduce oncoming wind velocities and help snow/sand particle deposition while preventing particle remobilization from excessive turbulent stresses.

Efforts concerning drag measurements will provide a bulk measurement of the wind fence resistance properties. The drag coefficients can facilitate understanding of effectiveness of wind fences along with detailed flow information. Future work suggestions entail a proper orthogonal decomposition (POD) analysis of flow fields to quantify vortices shed from wind fences in terms of kinetic energy contained. Also, exploring variations of fractal scaling parameters of the 2D fractal fence should give insight to optimal configurations for design of next generation wind fences.

REFERENCES

Anderson, D. A., Pletcher, R. H., and John C. Tannehill. "Reynolds Averaged Navier-Stokes Equations." Computational Fluid Mechanics and Heat Transfer. Third ed. Boca Raton: CRC, 2013. N. pag.272 Print.

Bailiang, Li, and Douglas J. Sherman. "Aerodynamics and Morphodynamics of Sand Fences: A Review." *Aeolian Research* 17 2015: 33-48.

Bitog, J. P., Lee, I.-B., Hwang, H.S., Shin, M.H., Hong, S.W., Seo, I.H., Mostafa, E., and Z. Pang. "A Wind Tunnel Study on Aerodynamic Porosity and Windbreak Drag". *Forest Science and Technology* 7:1 (2011): 8-16, DOI: 10.1080/21580103.2011.559939

Charonko, John J., and Pavlos P. Vlachos. "Estimation of uncertainty bounds for individual particle image velocimetry measurements from cross-correlation peak ratio". *Meas. Sci.Technol.* 24 065301 (26 April 2013): 16pp.

Clouds, River Networks. Digital image. *Fractals*. World of Mathematics, <http://world.mathigon.org/Fractals>.

Debnath, L. "A Brief Historical Introduction To Fractals And Fractal Geometry." *International Journal of Mathematical Education In Science & Technology* 37.1 (2006): 29-50. Computer Source. Web. 5 Oct. 2015.

Dierickx, W., Cornelis, W.M., and D. Gabriels. "Wind Tunnel Study On Rough And Smooth Surface Turbulent Approach Flow And On Inclined Windscreens." *Biosystems Engineering* 86 (2003): 151-166. ScienceDirect. Web. 5 Oct. 2015.

Dong, Z., Luo, W., Qian, G., and H. Wang. "Evaluating the optimal porosity of fences for reducing wind erosion*". Sciences in Cold and Arid Regions* 3.1: (2011): 1–12.

Gui, Lichuan, Wolfgang Merzkirch, and Ji-Zu Shu. "Evaluation of low image density recordings with the MQD method and application to the flow in a liquid bridge." *Journal of Flow Visualization & Image Processing* 4 (1997): 333-343.

Heisler, Gordon M., and David R. Dewalle. "2. Effects of windbreak structure on wind flow." *Agriculture, ecosystems & environment 22* (1988): 41-69.

Hurst, D., and J.C. Vassilicos. "Scalings and Decay of Fractal-generated Turbulence." *PHYSICS OF FLUIDS 19, 035103-1* (2007): *American Institute of Physics*, 13 Mar. 2007.

Kang, H, Duane D., and C. Meneveau. "Flow Over Fractals: Drag Forces And Near Wakes." *Fractals* 19.4 (2011): 387-399. Academic Search Complete. Web. 5 Oct. 2015.

Keylock, C. J., Nishimura, K., Nemoto, M., and Y. Ito. "The Flow Structure in the Wake of a Fractal Fence and the Absence of an “inertial Regime”. *Environmental Fluid Mechanics* 12.3 (2012): 227-50.

Kim, H. B., and S.J. Lee. "The Structure of Turbulent Shear Flow Around A Two-Dimensional Porous Fence Having A Bottom Gap." *Journal of Fluids and Structures* 16 (2002): 317-29.

Kljatov, Alexey. Snowflake. Digital image. 12 Stunning Snowflake Photos You Won’t Believe Were Taken by an Amateur Photographer. PBS, 28 Dec. 2015. Web. 11 Apr. 2016. <http://www.pbs.org/newshour/art/12-stunning-snowflake-photos-you-wont-believe-were-taken-by-an-amateur-photographer/>.

Kühn, W., J. Kompenhans, and J. C. Monnier. "Full Scale PIV Test in an Industrial Facility." *Particle Image Velocimetry*. Springer Netherlands, (2000): 91-150.

LaVision GmbH. “8 Vector Calculation Parameter: PIV.” *Flow Master Product-Manual for DaVis 8.2*. Göttingen: LaVision GmbH, 2013. 55.

LaVision Inc. PIV-Seminar USA 2014. PIV short course. Ypsilanti, Michigan. 21-23 Oct. 2014: 207, 221.

Lee, J., Lee, E., and S.J. Lee. "Shelter Effect of a Fir Tree with Different Porosities." *Journal of Mechanical Science and Technology* 28.2 (2014): 565-72. *Springer*.

Lee, S.J., and H. Kim. "Laboratory Measurements Of Velocity And Turbulence Field Behind Porous Fences." *Journal Of Wind Engineering & Industrial Aerodynamics* 80 (1999): 311-326. ScienceDirect. Web. 5 Oct. 2015.

Lee, S.J., Park, K., and C. Park. "Wind Tunnel Observations about the Shelter Effect of Porous Fences on the Sand Particle Movements." *Atmospheric Environment* 36.9 (2002): 1453-463.

Norem, Harald N. "Design criteria and location of snow fences." *Annals of Glaciology 6* (1985).

Perera, M. "Shelter behind two-dimensional solid and porous fences." *Journal Of Wind Engineering & Industrial Aerodynamics* 8. (January 1, 1981): 93-104. ScienceDirect, EBSCOhost (accessed October 4, 2015).

PIV Image Evaluation. Digital image. Particle Image Velocimetry. LaVision, Web. 19 Apr. 2016. <http://www.piv.de/piv/measurement_principle/page_1.php>.

Raffel, Markus, Christian E. Willert, and Jürgen Kompenhans. *Particle Image Velocimetry: A Practical Guide*. Berlin: Springer, 1998. 141. Print.

Raine, J.K., and D.C. Stevenson. "Wind Protection By Model Fences In A Simulated Atmospheric Boundary Layer." *Journal Of Wind Engineering & Industrial Aerodynamics* 2 (1977): 159-180. ScienceDirect. Web. 5 Oct. 2015.

Sciacchitano, A., Wieneke, B., and F. Scarano. "PIV uncertainty quantification by image matching". *Meas. Sci. Technol.* 24 045302 (2013).

Seoud, R. E., and J. C. Vassilicos. "Dissipation and decay of fractal-generated turbulence." *Physics of Fluids* (1994-present) 19.10 (2007): 105108.

Tabler, R. "Geometry and Density of Drifts Formed by Snow Fences." *Journal of Glaciology 26.94* (1980): 405-19. Web.

Tabler, R. "Design Guidelines For The Control Of Blowing And Drifting Snow." Washington, D.C.: *Strategic Highway Research Program, National Research Council*, (1994). *OhioLINK Library Catalog* – LR. Web. 1 Oct. 2015.

Tabler, R. "The Snow Fence Guide." Washington, D.C.: *Strategic Highway Research Program, National Research Council*, 1991, Report (SHRP-H-320), (1991). Web. 1 Oct. 2015.

Timmins, B.H, Wilson B.W, Smith B.L and P.P. Vlachos. "A method for automatic estimation of instantaneous local uncertainty in particle image velocimetry measurements" *Exp. Fluids* 53 (2012): 1133–47.

Tree as an Example of a Fractal We See and Take for Granted. Digital image. *Sustainable Organizing Milwaukee WI RSS*. BY-NC-SA 3.0 US, 18 Dec. 2013. Web. 11 Apr. 2016. <http://www.jenniferlinnig.com/wordpress/2013/12/planning-with-fractals-in-mind/>.

Wereley, S. T., L. Gui, and C. D. Meinhart. "Advanced algorithms for microscale particle image velocimetry." *AIAA journal* 40.6 (2002): 1047-1055.

White, F. M. (2011). Viscous fluid flow. New York, NY: McGraw-Hill Higher Education.

Wieneke, Bernhard. "PIV Uncertainty Quantification from Correlation Statistics." *Measurement Science and Technology* 26 (2015): 10pp.

Xue, Zhenyu, John J. Charonko, and Pavlos P. Vlachos. "Particle image velocimetry correlation signal-to-noise ratio metrics and measurement uncertainty quantification." *Measurement Science and Technology* 25.11 (2014): 115301.

APPENDIX

APPENDIX A

Comparison to literature

The 1D multi-scale fractal wind fence model in this present study was replicated from the first study on fractal wind fences by Keylock, et al., (2012). Therefore to compare results of the flow between the two as well as the wind fence of 2D multi-scale fractal structure, normalized streamwise velocity and turbulence intensity plots are graphically shown in Figure 40 for two downstream locations, 2.5H and 5H.

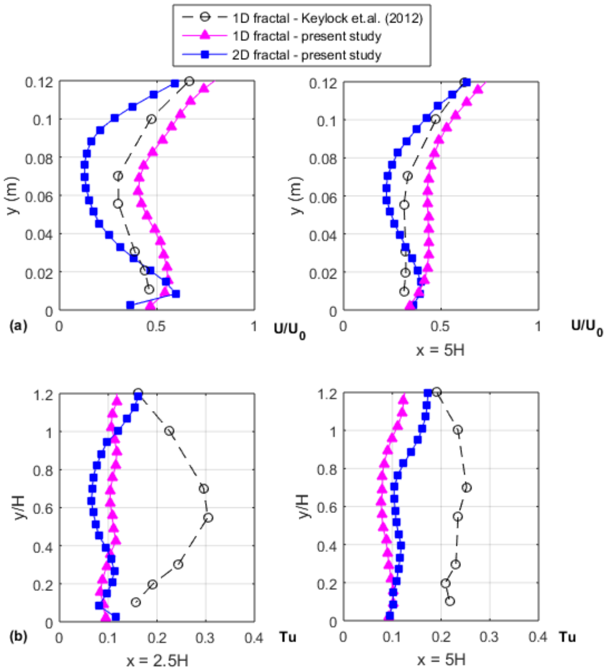

Figure 40: Vertical profiles of fractal wind fence models (a) normalized streamwise velocity and (b) normalized streamwise turbulence intensity

The two 1D fractal wind fence models do show some similarities in the shape of their vertical profiles along the fence height for the normalized streamwise velocity except for near the bottom surface. However, the vertical profiles along the fence height of the normalized streamwise turbulence intensity are not comparable. In addition, all of the four vertical profiles differ in magnitude. The differences in the magnitudes arise from the difference of the inflow condition between the two experiments. Furthermore, the detail of the vertical profiles differ because of the differences in the measurement techniques used.

Keylock, et al., (2012), used cross-wire anemometry which only provides point-wise measurements and requires an extensively longer time to collect data; therefore, fewer data points were obtained. Much more detailed vertical profiles were acquired for this study especially near the bottom surface, whereas Keylock, et al., (2012) began measurements at approximately y = 0.1H.

Laboratory measurements of the velocity and turbulence field behind two-dimensional porous fences (Lee and Kim, 1999) consisting of different porosities was used to compare the flow characteristics against the two-dimensional conventional (non-fractal) wind fence from this study. Because the previous study did not contain data for a 50% porosity fence, the data for the 40% and 65% porous fences were used to see if the measurements in this study fall somewhere in between. However, since 40% is closest to the 50% porosity fence in the study, the two vertical profiles along the fence height should theoretically be the most similar. Figure 41 shows vertical profiles to compare the (a) normalized streamwise velocity, (b) normalized vertical velocity, (c) normalized streamwise turbulence intensity and (d) normalized vertical turbulence intensity of the different porous (non-fractal) fences.

The normalized streamwise velocity in (a) among all the vertical profiles shown in (a)-(d) for the 40% and 50% porous fences show the most similarities except near the bottom surface. This difference is due to the presence of the conventional fence having a bottom gap whereas the fences in Lee and Kim, (1999) do not. Other discrepancies arise from the different inflow conditions between the two experiments. The experimental investigation of Lee and Kim, (1999) uses a circulating water channel where the boundary layer thickness is much smaller due to the density of water compared to the wind in the circulating wind-tunnel. Also, the porous fence models consist of different structural geometries and material which may have an effect. The shape of the voids in the fences used by Lee and Kim, (1999) consist of circular shapes where the voids in the conventional fence are squares.

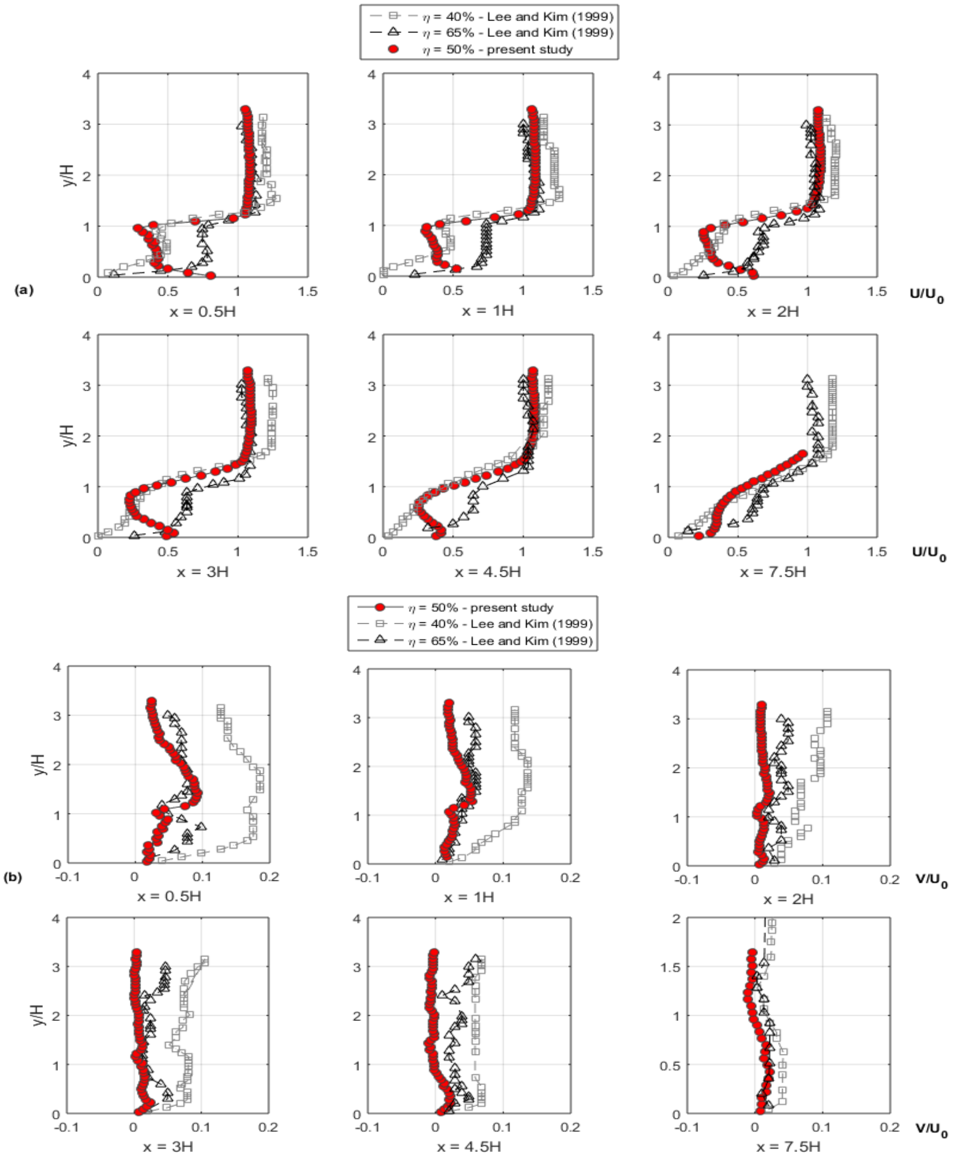

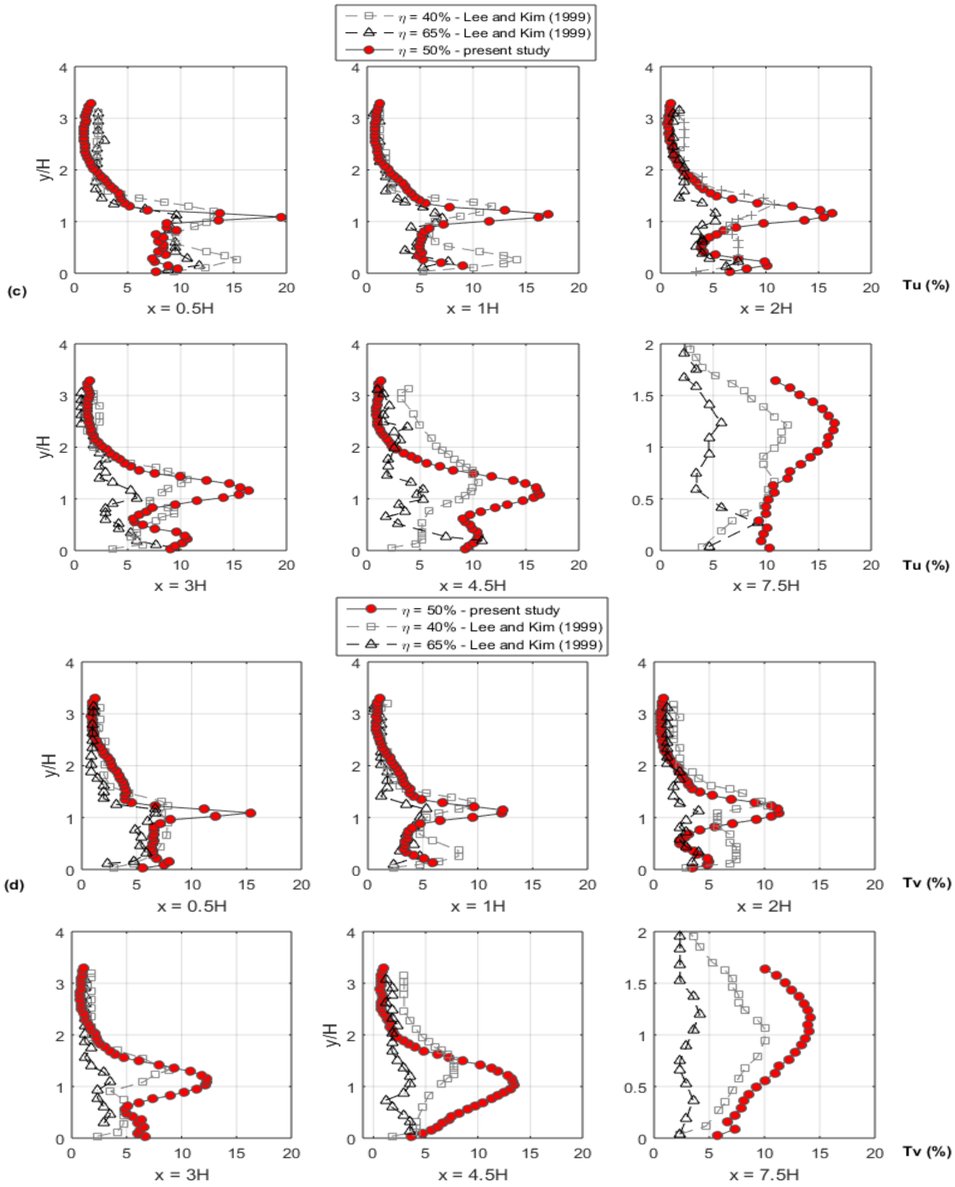

Figure 41: Comparisons of 2D conventional (non-fractal) porous wind fences (a) normalized streamwise velocity, (b) normalized vertical velocity, (c) normalized streamwise turbulence intensity and (d) normalized vertical turbulence intensity

APPENDIX B

Matlab code for ensemble averaged mean flow properties and turbulent statistics

```
U0=5.53;   % freestream velocity
H=100; %mm
directory_1= vector folder
suffix='*.dat'; %*.bmp or *.tif or *.jpg
pixelSize = (10/106); %(mm/pixel)
newtextdata={'VARIABLES =
"x","y","meanu","meanv","stdU","stdV","Tu","Tv","TKE","RSS"'};
dt = 0.00012;
direc_1 = dir([directory_1,filesep,suffix]);
filenames_1={};    % Cell
[filenames_1{1:length(direc_1),1}] = deal(direc_1.name);
filenames_1 = sortrows(filenames_1); % sort all image files
amount_1 = length(filenames_1);
k=0;
for Num= 1:1:1147
   DELIMITER = ' ';
   HEADERLINES = 3;
   newData1 = importdata(fullfile(directory_1, filenames_1{Num}), DELIMITER,
HEADERLINES);
   vars = fieldnames(newData1);
       for i = 1:length(vars)
          assignin('base', vars{i}, newData1.(vars{i}));
       end
   k=k+1;
   dataa(:,:,k)=data;   % dat header
end
realU=dataa(:,3,:).*(1/10600)./dt;    %m/s
realV=dataa(:,4,:).*(-1/10600)./dt;    %m/s
meanU=mean(realU,3);
meanV=mean(realV,3);
StdU=std(realU,1,3);
StdV=std(realV,1,3);
for i = 1:1147       % Number of instantaneous velocity fields
     U_prime(:,1,i) = realU(:,1,i)-meanU(:,1);
     V_prime(:,1,i) = realV(:,1,i)-meanV(:,1);
     UV_prime(:,1,i) = -(U_prime(:,1,i).*V_prime(:,1,i));
end
RSS=mean(UV_prime,3)./U0^2;  %Reynolds Shear Stress, RSS
VarU = var(realU,1,3);
VarV = var(realV,1,3);
TKE = (1/2).*(VarU+VarV); %Turbulence kinetic energy, K
Tu = (abs(StdU./U0))*100;   %Streamwise turbulence intensity, Tu(%)
Tv = (abs(StdV./U0))*100;   %Vertical turbulence intensity, Tv(%)
```